Low Threshold Current Strained InGaAs/AlGaAs Quantum Well Lasers

Thesis by

Lars E. Eng

In Partial Fulfillment of the Requirements
for the Degree of
Doctor of Philosophy

California Institute of Technology
Pasadena, California
1993
(Defended May 14, 1993)

To my Mother and Father

Acknowledgments

I would first like to acknowledge the support and encouragement of my advisor, Professor Amnon Yariv. I appreciate the opportunity to have been part of his group and interact with the first rate students, staff, and visiting scientists in the environment he has provided. I am very fortunate to have had the chance to work with Professor Hadis Morkoç who generously shared his wealth of MBE knowledge during his stay at Caltech. I would also like to thank the following:

Dr. Steve Sanders for making laser processing more enjoyable, many helpful discussions and collaborations, and helping arrange a first date with Julie.

Dr. Anders Larson for helpful and open MBE discussions, and lending spare parts when I needed them.

Dr. David Mehuys, Dr. Hal Zarem, and Dr. Kazumasa Mitzunaga for guidance and collaborations in my first few years.

Dr. T.R. Chen, and Y.H. Zhuang for LPE fabrication, processing expertise, and collaborations.

Ilan Grave, Dr. Michael Mittelstein, and Dr. Amir Sa'ar for collaborations.

Ali Shakouri and John O'Brien for stimulating discussions and proofreading of this thesis.

Ali Ghaffari for dedicated work on the MBE system.

Former MBE group members Naohiro Kuze, Yoshihiro Yamada, Dr. Sidney Kan, Dr. Howard Chen, and Dr. Pam Derry.

Thomas Schrans, Randal Salvatore, and Dr. Joel Paslaski for helpful discussions.

Desmond Armstrong and Kevin Cooper for building and trouble shooting electronics.

Jana Mercado for her day to day help and cheerful demeanor.

I would like to thank my family, Mom, Dad, Bjorn, Maria, Ingrid, Mats, and Louise for supporting me through all the ups and downs in graduate school. Many thanks also to my second family, Tom, Terri, Sandy, and Lindsey Soderstrom.

Finally, I want thank Julie Sheridan for her cheerleading and her unconditional love all these years.

Abstract

Strained InGaAs quantum well lasers offer the prospect of lower threshold currents, higher modulation speed, and lower linewidths than lattice matched GaAs quantum well lasers. In addition, the useful wavelength region of the GaAs material system is extended from $0.87\mu m$ to beyond $1\mu m$ with the addition of indium to the quantum well.

The lasers are fabricated using Molecular Beam Epitaxy (MBE) for the semiconductor layer structure. Liquid Phase Epitaxy (LPE) is then used to provide lateral optical mode and current confinement. Broad area threshold current densities of $J_{th} = 114\frac{A}{cm^2}$ is the first demonstration of high quality MBE grown strained InGaAs laser material. Measured transparency currents of $25\frac{A}{cm^2}$ are a factor of two lower than in GaAs, which is consistent with a lower valence band density of states in the strained material. Buried heterostructure lasers made from this material with $2\mu m$ wide stripe widths lase with a minimum threshold of $1.0mA$ (CW), the lowest value for a single quantum well laser with as-cleaved mirrors in any material system. With high reflectivity coatings (R=0.9) the first sub milliampere strained InGaAS lasers are obtained, with $I_{th}^{min} = 0.35mA$. Details of the material growth, device fabrication, and device optimization are presented.

The broad gain bandwidth of single quantum well lasers is used to tune the lasing wavelength of optimized GaAs lasers over 125 nm and InGaAs lasers over 170 nm in an external cavity configuration. The measured tuning curves obtained for the InGaAs lasers are qualitatively different, and the difference can be attributed to the modified strained valence band strucure.

Low temperature ($5^\circ K$) performance of low threshold lasers is investigated. The decrease in threshold with temperature is found to be linear over a range of $200^\circ K$ for both GaAs and InGaAs with a larger decrease in threshold for the GaAs case. This result agrees well with a lowered valence band effective mass in the strained laser.

Contents

Chapter 1

Low Threshold Semiconductor Lasers

1.1 Introduction

The needs of the telecommunications industry have been responsible for much of the research on semiconductor diode lasers over the past two decades. Due to their small size, high modulation speed, and wavelength tailorability, these lasers are ideal as a source to send information as modulated light down optical fibers in high data rate communication systems. The superior bandwidth of fibers over electrical coaxial cables has resulted in communication links with data transmission rates above 1 Gbit/s.

Optical data storage and retrieval, most notably within the audio and video compact disc industry, is another area of active research in semiconductor lasers. Here, speed is not as important as the small size and low cost. The main effort in this area is to reduce the lasing wavelength in order to increase the data packing density.

The systems mentioned above use a single, or only a few, discrete laser diodes. For future computer interconnects, however, thousands of lasers will be necessary for parallel chip to chip optical interconnects. In large scale integration schemes using lasers together with electronic devices, the current necessary to turn on the laser, the threshold current, is the major source of power dissipation. For practicle large scale systems, this current must be below 1 mA.

The approach to lowering laser threshold current amounts to reducing the number of injected electrons necessary required for population inversion, as well as minimizing the losses experienced by the optical field. Optimum laser performance for low threshold is achieved by shrinking the physical dimensions of the laser and lowering the optical mode loss by increasing the mirror reflectivity and fabricating low loss waveguides.

1.2 GaAs Quantum Well Lasers

With modern semiconductor crystal growth techniques, such as Molecular Beam Epitaxy (MBE) and Metal Organic Vapor Deposition (MOCVD), it is possible to grow semiconductor laser structures with active region thicknesses of less than 100 Angstroms. In this regime, quantum size effects can be observed and the electron density of states is modified compared with the bulk material. Due mainly to the thin active region, the threshold current can be reduced by over an order of magnitude compared with bulk lasers. The predicted lower limit to the threshold current for an optimized single quantum well laser with realistic losses is $I_{th}^{min} = 0.1mA$ [1]. Threshold currents of 0.55 mA have been measured for a buried heterostructure (BH) GaAs single quantum well laser with high reflectivity coatings [13,12]. Other geometries, such as vertical cavity surface emitting lasers [5,5,6] and narrow stripe structures on patterned substrates [7,9] have also produced thresholds below 1 mA.

1.3 Strained InGaAs Quantum Well Lasers

By adding indium to the GaAs active region, making an InGaAs alloy, the band gap is lowered and increases the lasing wavelength range to beyond $1\mu m$. This wavelength region is particularly attractive since Er^+ doped fiber amplifiers used in state-of-the-art communication systems are efficiently pumped at a wavelength of 980 nm. Because of the lowered band gap, the barrier heights to the quantum well can be made higher leading to more efficient current injection. By the same measure, the available index step for a given barrier height is larger, resulting in an increase in optical confinement factor which increases the modal gain.

However, the lattice constant of InAs ($a_0 = 6.0584\mathring{A}$) is 7% larger than that of GaAs ($a_0 = 5.6533\mathring{A}$), so for InGaAs to be grown dislocation free on a GaAs lattice, it will be under compressive strain. Matthews [16] has shown that a stable strained crystal can be grown as long as the layer is thin enough. The first demonstration of a current injected strained InGaAs laser structure was demonstrated in 1984 [11]. The threshold current densities for these devices were over $1000\frac{A}{cm^2}$, more than 5 times higher than similar unstrained GaAs results. Yablonovich and Kane [1] and Adams [2] calculated the energy band structure of strained layers and showed that strain should actually enhance laser performance. The effect of strain is to split the degenerate valence band energies and lower the effective hole mass to near that of a conduction electron. This in turn will lead to a lower inversion condition, less loss due to intervalence band absorption, and the prospect of lower threshold currents.

This thesis presents the theory, growth, and fabrication of sub milliampere threshold current strained InGaAs/AlGaAs quantum well lasers. Threshold currents for as-cleaved lasers of 1.65 mA are the lowest reported for a single quantum well laser in any material system. With high reflectivity coatings the threshold is reduced to 0.75 mA, which is a record for this material system and rivals the best results of unstrained GaAs lasers [11,2].

1.4 Outline of Thesis

Chapter 2 describes the MBE crystal growth system used to grow the epitaxial laser structures used in this work. Considerations for high quality InGaAs growth are discussed, as well as an approach to obtaining growth rates to within 2% accuracy.

Chapter 3 provides the theoretical background and calculations of energy levels, density of states, and gain in a strained single quantum well with AlGaAs barriers.

Differences between GaAs and InGaAs gain are highlighted.

In chapter 4 the details of the InGaAs laser structure are given. The experimental method for optimizing the laser for low threshold is given. Record low threshold currents of of 1.65 mA (CW, R = 0.3) and 0.75 mA (CW, R = 0.9) are obtained.

In chapter 5 the broadband gain properties of a single quantum well is taken advantage of to tune the lasing wavelength over a record wide range of 170 nm [17]. A comparison with optimized GaAS lasers tuning curves is made.

Chapter 6 describes measurements of laser threshold at low temperatures [18]. Thresholds are reduced to the microampere range, with a larger reduction in GaAs than InGaAs.

References

[1] A.Yariv, *Appl. Phys. Lett.* **53**, 1033 (1988)

[2] P. Derry, A. Yariv, K. Lau, N. Bar-Chaim, K. Lee, and J. Rosenberg, *Appl. Phys. Lett.* **50**, 1773 (1987)

[3] K.Y. Lau, P.L. Derry, and A. Yariv, *Appl. Phys. Lett.* **52**, 88 (1988)

[4] J. Jewell, J.P. Harbison, A. Scherer, Y.H. Lee, and L.T. Florez, *J. Quant. Electr.* **27**, 6, 1332 (1991)

[5] K.Tai, R.J. Fischer, C.W. Seabury, N.A. Olsson, T. Hou, Y. Ota, and A. Cho, *Appl. Phys. Lett.* **55**, 2473 (1989)

[6] R.S. Geels, S.W. Corzine, J.W. Scott, D.B. Young, and L.A. Coldren, *IEEE Photn. Techn. Lett.* **2**, 234 (1990)

[7] E. Kapon, C.P. Yun, J.P. Harbison, L.T. Florez, and N.G. Stoffel, *Electron. Lett.* **24**, 985 (1988)

[8] E. Marclay, D.J. Arent, C. Harder, H.P. Meier, W. Walter, and D.J. Webb, *Electron. Lett.* **25**, 892 (1989)

[9] D.J. Arent, L. Brovelli, H. Jackel, E. Marclay, and H.P. Meier, *Appl. Phys. Lett.* **56**, 20, 1939 (1990)

[10] J.W. Matthews and A.E. Blakeslee, *J. Cryst. Growth* **27**, 118 (1974)

[11] W.D. Laidig, P.J. Caldwell, Y.F. Lin, and C.K. Peng, *Appl. Phys. Lett.* **44**, 653 (1984)

[12] E. Yablonovich and E.O. Kane, *J. Lightwave Tech.* **LT-4**, 504 (1986)

[13] A.R. Adams, *Electron. Lett.* **22**, 249 (1986)

[14] I. Suemune, L.A. Coldren, M. Yamanishi, and Y. Kan, *Appl. Phys. Lett* **53**, 1378 (1988).

[15] L.E. Eng, T.R. Chen, S. Sanders, Y.H. Zhuang, B. Zhao, H. Morkoç, and A. Yariv, *Appl. Phys. Lett.* **55**, 1378 (1989).

[16] T.R. Chen, L.E. Eng, Y.H. Zhuang, and A. Yariv, *Appl. Phys. Lett.* **56**, 11, 1002 (1990)

[17] L.E. Eng, D.G. Mehuys, M. Mittelstein, and A. Yariv *Electron. Lett.* **26**, 1675 (1990)

[18] L.E. Eng, A. Sa'ar, T.R. Chen, I. Grave, N. Kuze, and A. Yariv, *Appl. Phys. Lett.* **58**, 2752 (1991)

Chapter 2

Molecular Beam Epitaxy of GaAs, InGaAs, and AlGaAs for Optoelectronic Devices

2.1 Introduction

All epitaxial III-V semiconductor layers described in this thesis have been grown by Molecular Beam Epitaxy (MBE). A brief description of the growth system and process, and some key problems encountered are presented in this chapter. It is shown that if care is taken, absolute layer thicknesses can be controlled to within 2%. A complete review of the growth technique and process can be found in review articles in references [1]-[4].

2.2 MBE Growth: An Overview

MBE is a crystal growth technique used to grow epitaxial layers of semiconductor crystals. Effusion cells containing the constituent materials (Ga,Al,In,As) and dopants (Si,Be) are pointing, in the horizontal plane, toward the heated substrate near the chamber center. By heating the sources to their evaporation temperatures, molecular beams are thus created which impinge on the GaAs substrate and recombine to form crystalline III-V material at the substrate surface. Because the beams hit the substrate at an angle, the substrate is rotated azimuthally during growth which results in approximately 10% uniformity across the wafer. The growth parameters in an MBE process include the choice of arsenic species (As_2 or As_4), the ratio of As to group III flux, and the substrate temperature. The alloy composition (for random alloys) is controlled by the cell temperatures, and the beams are turned on or off using mechanical shutters in front of each cell. The alloy composition, x, for $Al_xGa_{1-x}As$ is given by

$$x = \frac{R_{AlAs}}{R_{AlAs} + R_{GaAs}} \tag{2.1}$$

where R denotes the incorporation rate of the material into the crystal. Because of the low fluxes, possible growth rates can vary from fractions of, to a couple of, microns per hour. This translates to a rate on the order of one atomic layer per second. This property makes MBE an ideal growth technique where layer thicknesses with precision to atomic scales, with monolayer roughness, is desired.

2.3 System Specifics

The system used in our laboratory is a RIBER 2300 three chamber system with 2" wafer capability. Many of the characteristics of crystal growth, such as uniformity, vacuum, and cell temperature stability, are system dependent. All chambers are under ultra high vacuum (UHV), pumped with ion pumps. Two of the chambers serve primarily as sample introduction chambers, or load locks, so that the integrity of the vacuum in the growth chamber is maintained. A cross section of the growth chamber is shown in Figure 2.1. During growth, the pumping speed is increased by filling the cryopanels, or shrouds, with liquid nitrogen (LN_2), and pressures in the 10^{-10} Torr range are achieved. The growth chamber is exposed to atmospheric pressure only when the material in the cells are depleted or a crucial part of the hardware breaks down and the system must be rejuvenated. After this, several weeks of baking, degassing, and calibration are required to grow crystals with a purity demanded by optoelectronic devices. In fact, a good measure of the cleanliness of the system is the threshold current of a broad area "standard design" single quantum well laser, which should be below $400\frac{A}{cm^2}$. As long as no mechanical difficulties are encountered, the time between venting can be longer than eight months, or after several hundred μm of material growth. The system is equipped with a large volume (200 cc) arsenic (As) cracking cell (Perkin-Elmer 06-200) which can be used to generate As_2, As_4, or a mixture of the two. The growth is always done with an excess of arsenic to prevent group III island formation. The growth rate is thus determined by the arrival rate of

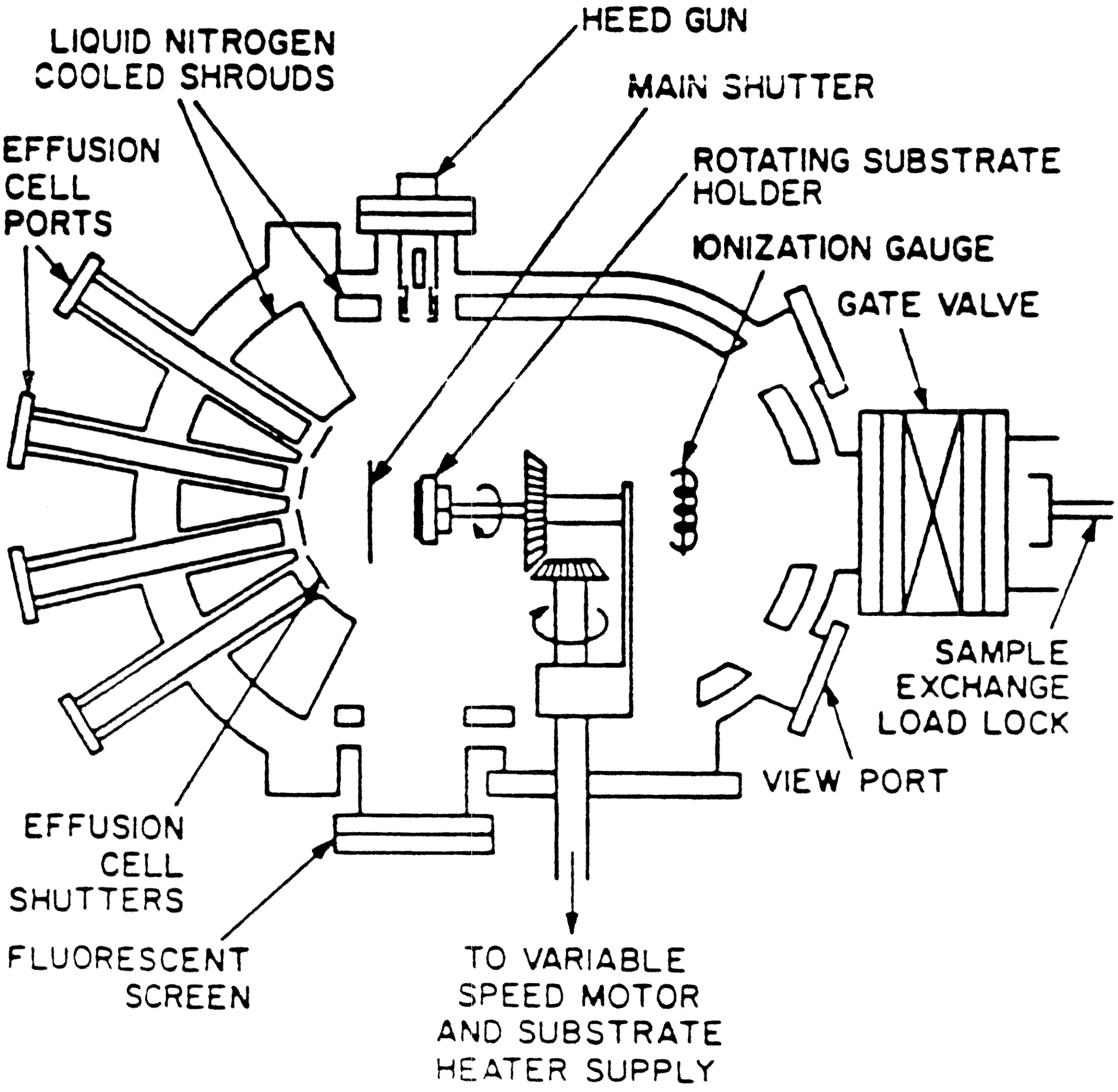

Figure 2.1: A schematic of the RIBER 2300 MBE growth chamber.

group III atoms, and the excess arsenic is re-evaporated from the surface. Keeping the arsenic overpressure to a minimum not only conserves source material but also improves the crystal quality.

An optimum substrate temperature must also be found for each material or alloy. The choice of this temperature is often a trade off between sharp interfaces with controlled growth rates and background impurity incorporation. To obtain high luminescence efficiency, for instance, may require growing the material at a substrate temperature higher than would be chosen to obtain the sharpest interfaces.

2.4 Precise Growth Rates in MBE

The trend in semiconductor devices is toward smaller and smaller dimensions to lower power requirements. In the past six years, a new class of devices based on microcavity resonators has emerged. This class includes Fabry Perot cavity devices with epitaxially grown distributed Bragg reflectors (DBR), such as optical modulators and vertical cavity surface emitting lasers (VCSEL) whose size is on the order of a wavelength of light. In these devices the entire cavity is grown in the MBE. A high finesse cavity (high R mirrors) requires a large number of mirror pairs of very controlled thickness. Thus, the growth time is very long, often 6-8 hours, and growth rates must be controlled to better than 2%. Previous to this class of device, this amount of precision has not been necessary in MBE growth. Although MBE allows interface sharpness to be made on the order of 1 atomic layer, a great deal of care must be taken in calibrations and growth rate monitoring to assure an absolute layer thickness accuracy of better than 10%.

Our MBE, like most, is equipped with an ionization gauge which can be rotated into the path of the molecular beams for flux measurements. The gauge sensitivity to the different materials is known and the measured beam pressures can be converted to beam fluxes with this data. It may seem that this would be a simple way to monitor growth rates. In practice, however, we notice large variations in the measured fluxes (due to gauge sensitivity variations) from one day to the next. Therefore, this method only allows us to measure growth rates to within an order of magnitude.

The next simplest method is to grow several thick layers, measure the thicknesses with a scanning electron microscope (SEM) and plot the growth rate vs. $\frac{1}{T_{cell}}$ on a log scale. Using the vapor pressure curve to fit the data, it is possible to interpolate or extrapolate growth rates with about 10% accuracy.

The most precise way to measure growth rates is to use Reflection High Energy Electron Diffraction, or RHEED, intensity measurements. An electron gun is present in the chamber and electrons are accelerated towards the sample at a shallow incident angle and diffracted onto a phosphorous screen as shown in Figure 2.1. The intensity of the specularly reflected electron beam is monitored with a Si photodiode followed by a current amplifier. It has been shown [2] that this intensity oscillates with the period corresponding precisely to one atomic layer of growth. Some typical RHEED data is shown in Figure 2.2. Typically the oscillations are damped so it is only possible to measure the growth rates for the first 10 - 30 monolayers.

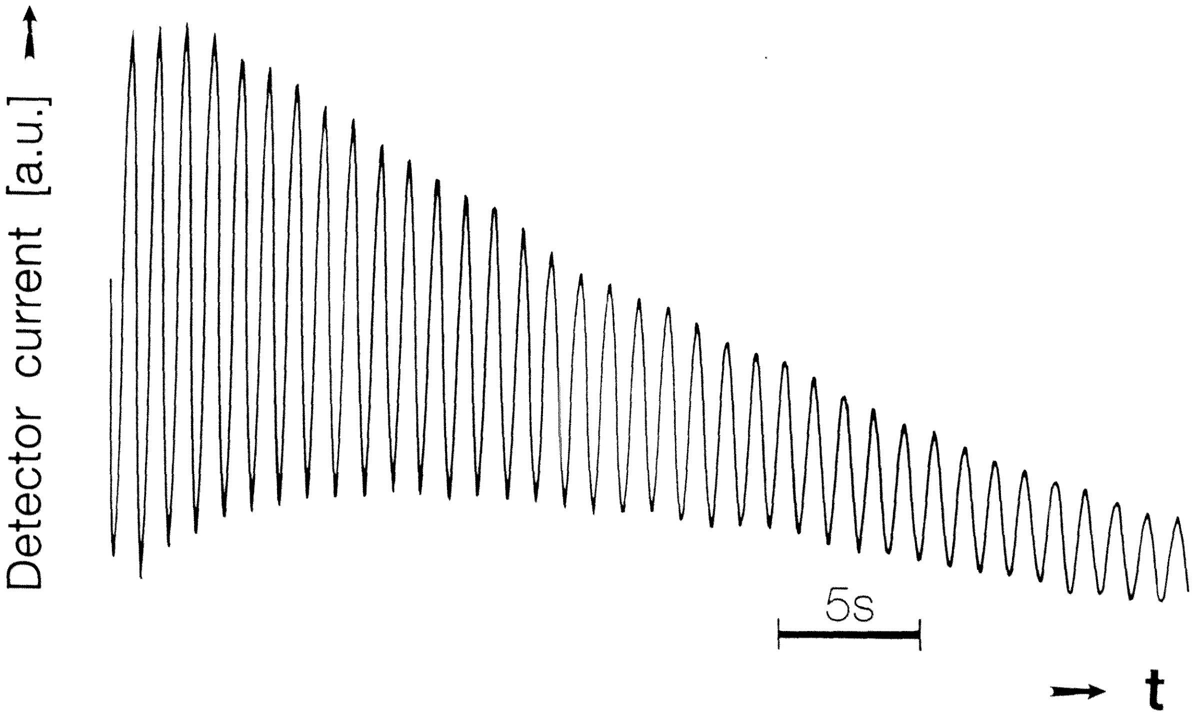

Figure 2.2: Measured oscillations in the specular reflected RHEED beam after initial growth of AlAs (the aluminum shutter is opened at t=0). The corresponding growth rate is approximately 1 monolayer per second.

The cells experience a different environment when the shutter is closed than when it is open. This leads to a decrease in cell temperature, and therefore growth rate, with time. A measurement of the aluminum and gallium cell fluxes versus time after opening the shutter in front of the cell is shown in Figure 2.3. It is clear that the flux undergoes a transient and is up to 15% higher at t=0 than it is in steady state. Therefore, the RHEED oscillation measurement is very sensitive to the state of the cell before opening. We have developed a technique to reproducibly measure growth rates from RHEED. We open the shutter in front of the cell while keeping the main shutter closed for two minutes. This gives the cell time to equilibrate and reproduce a steady state flux. We then begin to record oscillations as the main shutter is opened. In this way we can find the steady state growth rate for each cell at a given cell temperature. By knowing the transients from the flux measurements, we therefore know the growth rate at any time. The use of 1" spacers between the cells and growth chamber increases the distance between the shutter and cell and has been shown to reduce growth rate transients significantly [8,8]. In our system we have measured a decrease in flux transients from 15% to 4% when using the spacers.

If we look at the gallium flux in Figure 2.3, we notice random fluctuations of a few percent, which we don't see in any of the other cells. Other researchers [9] have seen this effect as well and attribute it to gallium "spitting." They have been able to eliminate this problem with a modern cell design. If the cell has not been modified, it is important that these variations average out over the time it takes to grow one layer. If they do not, the growth rate will vary from layer to layer, and no amount of

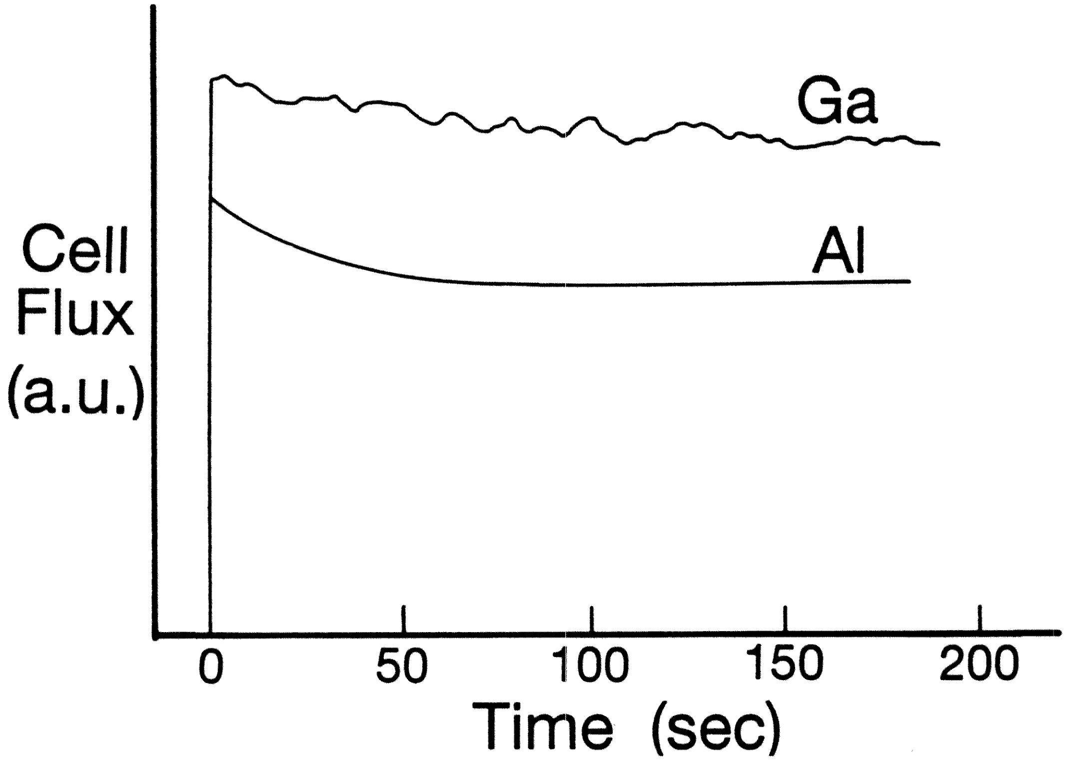

Figure 2.3: Beam fluxes for a) aluminum and b) gallium cells vs. time after shutter opening. Note the random fluctuations in the gallium flux.

calibration will be sufficient to grow high finesse Fabry Perot resonators.

2.5 Cell Flux Stability

Any variations in cell temperature will cause variations in the growth rate. Therefore, since we have a strict limit how much the growth rate can vary, we need to determine the allowable temperature variation. Within the temperature range of interest, the cell flux, and therefore the growth rate R, can be related to the cell temperature through the relation

$$R = Ae^{-\frac{B}{T}} \tag{2.2}$$

where A and B are constants which depend on the material, and the temperature is in degrees Kelvin. These constants can be found by knowing growth rates at two different cell temperatures. As an example of the flux stability with temperature, for our aluminum cell ($B = 3.8310^4 [^\circ K]$) we require a cell temperature stablility $\Delta T < 0.5^\circ K$ at $1135^\circ C$ for a flux variation $\frac{\Delta R}{R} < 1\%$.

2.6 Reproducible Growth Rates

We have found that the growth rates vary up to 10% from one day to the next. Therefore, it is necessary to develop a procedure to determine the growth rate immediately before growing a particular device. In order to accurately determine the rate, it is necessary to grow structures which are sensitive to small fluctuations in layer thicknesses. Periodic reflective structures, Bragg reflectors, are sensitive to variations of

$< 1\%$. Before growing a new device structure, we grow a Bragg reflector, measure the spectral reflectance, and compare with the predicted curve. The difference between the designed and measured data gives us a factor by which to multiply the RHEED oscillation data. In Figure 2.4 we show measured reflectance, $R(\lambda)$, for a Fabry-Perot cavity grown by the above procedure. The designed transmission peak was 950 nm, and the measured peak was 937.5 nm, an error of less than 2%. The half width of the transmission peak, which is a measure of the reflectivity, was also within experimental error. The calculation of the reflectivity was done using the matrix method for wave propagation in multilayered structures [11], and the refractive index data for GaAs and AlGaAs was taken from reference [12]. In Figure 2.5 we show the reflectance of a vertical cavity surface emitting laser grown by this technique. Note the narrow dip at 881 nm. Losses in the cavity and nonuniformity over the sampled area limit the depth of the dip. Also shown is the lasing peak of this structure under optical excitation.

The above calibration techniques are only useful if the sticking coefficients of the group III atoms are constant during growth. Gallium, indium, and aluminum all have different critical temperatures, T_{crit}, above which the sticking coefficient becomes less than unity. Above this temperature, the growth rate becomes extremely sensitive to substrate temperature as well as the presence of other group III elements at the substrate surface [13], and is not easily controlled. Recent work [14,15] have experimentally determined $T_{crit} = 540°C$ for InAs growth on GaAs, with desorption rates of $10 - 25\%$ at a substrate temperature of $600°C$. If grown at too low temperature,

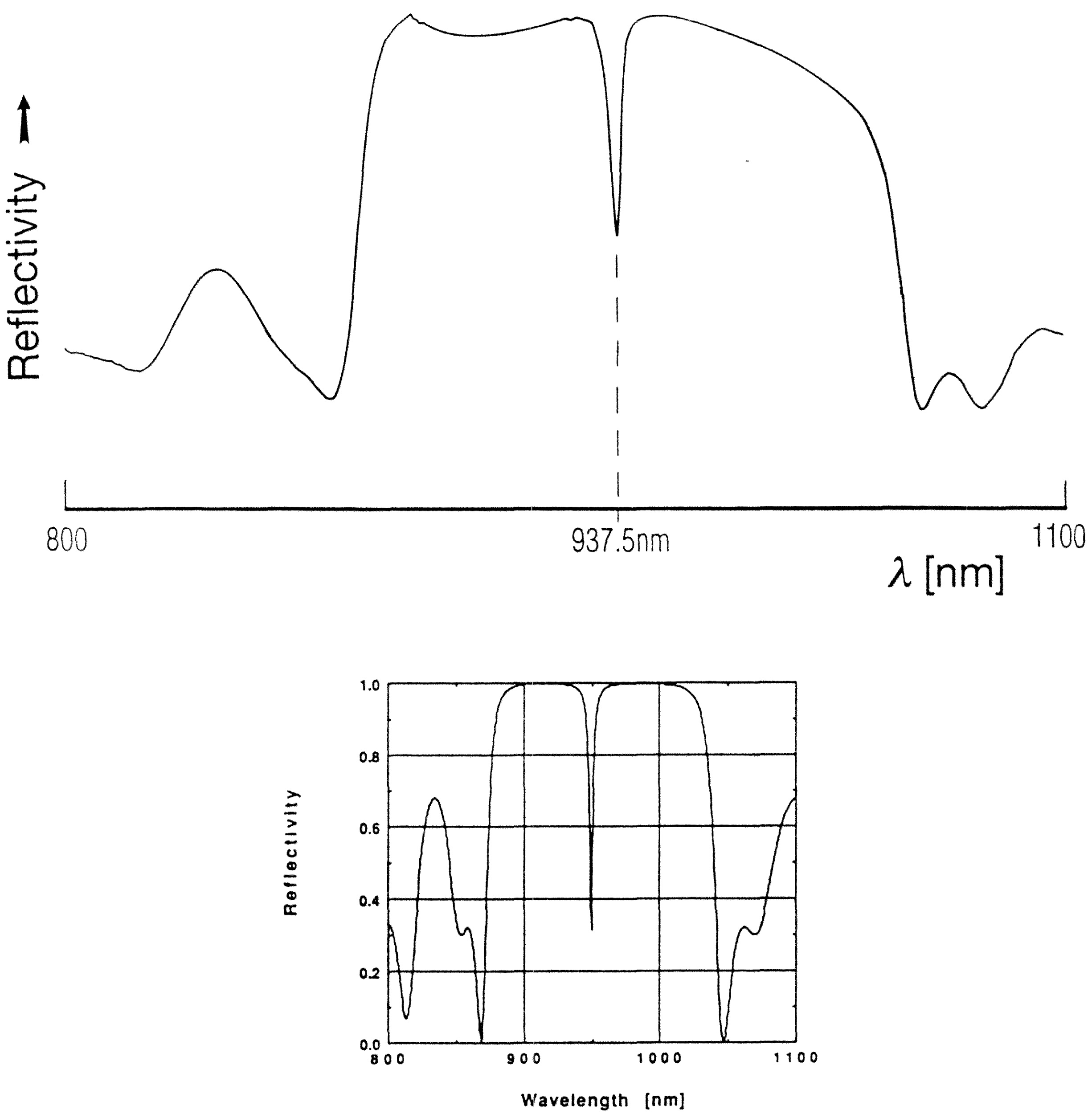

Figure 2.4: a) Measured and b) calculated reflectance spectra for a passive, i.e. no gain medium, Fabry-Perot cavity grown by MBE.

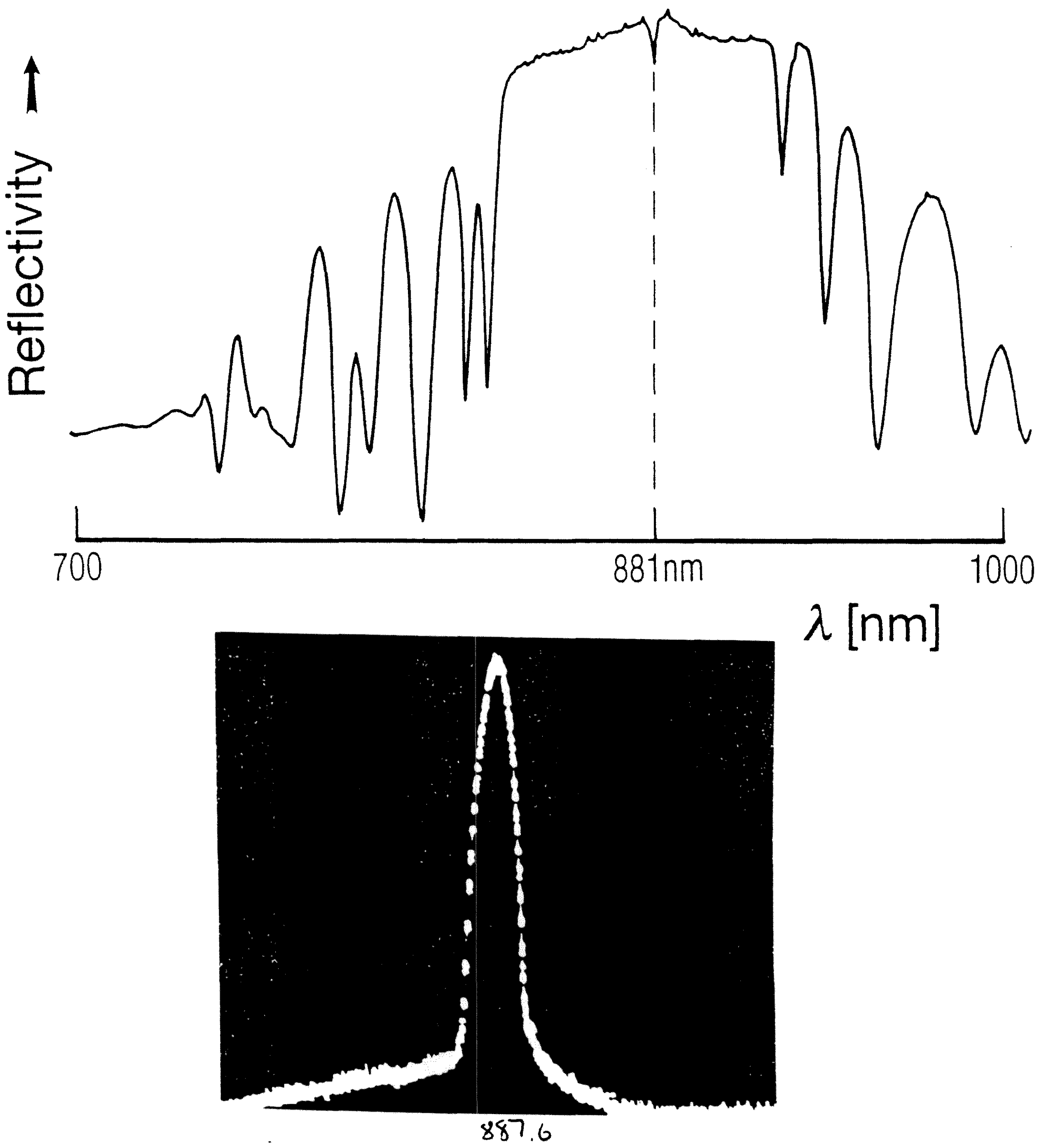

Figure 2.5: a)Measured reflectance spectra for a VCSEL structure cavity grown by MBE. b) Lasing emission from the VCSEL pumped optically.

however, the luminescence efficiency of the crystal is drastically reduced. A compromise has to be made in which a trade off between crystal purity and growth rate accuracy is considered.

2.7 InGaAs Growth

The growth of InGaAs on GaAs places a restriction on the maximum layer thickness while still retaining dislocation-free material, since the lattice constants of InAs ($a_0 = 6.0584A$) and GaAs ($a_0 = 5.6533A$) differ by more than 7%. However, if the layers are thin enough [16], the in-plane lattice miss-match is accomodated by strain, $\epsilon_{||}$, defined as

$$\epsilon_{||} = \frac{a_0^{In_xGa_{1-x}As} - a_0^{GaAs}}{a_0^{GaAs}}$$

when the strained layer takes on the lattice constant of the substrate. The free-standing lattice constant of InGaAs is taken as a linear interpolation of GaAs and InAs lattice constants

$$a_0^{In_xGa_{1-x}As} = 5.6533 + 0.405x.$$

Matthews and Blakeslee [16] have derived expressions for the maximum layer thickness, the critical thickness, beyond which the energy of forming a dislocation is equal to the amount of strain energy in the film. In practice [15] this limit is in reasonable agreement with observed photoluminescence efficiency in strained InGaAs layers. Figure 2.6 shows the calculated critical thickness for InGaAs grown on GaAs as a function of indium concentration using this model. The practical limit of x for single

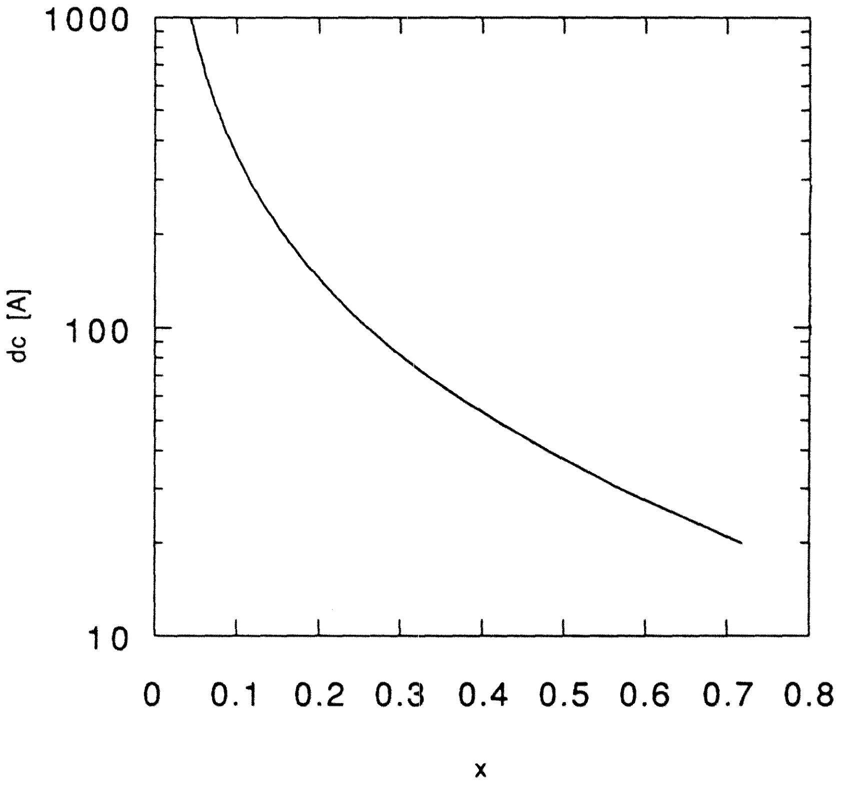

Figure 2.6: Calculated critcal layer thickness for strained InGaAs on GaAs using Matthews and Blakeslee model [16] as a function of indium content.

InGaAs quantum wells is 40% for reasonable well widths ($d > 40\mathring{A}$).

2.8 Conclusions

We have shown that MBE can give very precise growth rates. For many structures, such as edge emitting quantum well lasers, crystal purity is much more important than accuracy. However, devices based on interference reflectors and filters require thickness fluctuations of less than 2 % over growth times of 6 - 10 hours. In order to obtain growth rate accuracy better than 10 %, it is essential to ensure long term cell flux stability over the entire growth. It is also necessary to compensate for the growth rate transients either by reducing them as much as possible, or by accounting for them with averaged growth rates.

References

[1] A.Y. Cho, *Thin Solid Films* **100**, 291 (1983)

[2] C.T. Foxon, *Acta Electronica* **21**, 2, 139 (1978)

[3] B. Joyce, *Rep. Prog. Phys.* **48**, 1637 (1985)

[4] K. Ploog, *Ann. Rev. Mat. Sci.*, 171 (1981)

[5] J. Jewell, J.P. Harbison, A. Scherer, Y.H. Lee, and L.T. Florez, *J. Quant. Electr.* **27**, 6, 1332 (1991)

[6] Riber operators manual

[7] A. Larsson, private communication

[8] J.S. Harris, private communication

[9] J. Miller, *J. Vac. Sci. Tech.* **B**, 10, 803 (1992)

[10] W.T. Tsang, F.K. Reinhart, and J.A. Ditzenberger, *Appl. Phys. Lett.* **36**, 118 (1980)

[11] P. Yeh, *Optical Waves in Layered Media*, Wiley (1988)

[12] Afromovitz, *Solid State Comm.* **15**, 59 (1974)

[13] R. Fischer, J. Klem, T.J. Drummond, R.E. Thorne, W. Kopp, H. Morkoç, and A.Y. Cho, *J. Appl. Phys.* **54**, 2508 (1983)

[14] M.T. Emeny, L.K. Howard, K.P. Homewood, J.D. Lambkin, and C.R. Whitehouse *J. Crystal Growth* **111**, 413 (1991)

[15] J.P. Reithmaier, H. Riechert, H. Schlotterer, and G. Weimann, *J. Crystal Growth* **111**, 407 (1991)

[16] J.W. Matthews and A.E. Blakeslee, *J. Cryst. Growth* **27**, 118 (1974)

[17] J.E. Schirber, I.J. Fritz, and L.R. Dawson, *Appl. Phys. Lett.* **46**, 187 (1985)

Chapter 3

Model for Gain and Threshold Current in GaAs and Strained InGaAs Quantum Well Lasers

3.1 Introduction

In this chapter, the expression for gain as a function of photon energy is presented for a quantum well laser structure. The equation is given in terms of the density of states in the conduction and valence bands, the interband matrix element, and carrier injection level, assuming that the k-selection rule holds. The addition of indium to a GaAs quantum well introduces strain due to the lattice mismatch between InAs and GaAs. The built-in strain has been shown to increase the band gap as well as split the degenerate heavy and light valence band edges. This reduces the interaction between valence bands, resulting in a lower valence band density of states compared with unstrained GaAs quantum wells [14,13]. Calculations of a realistic laser structure, assuming parabolic bands, an energy- and material-independent matrix element, and a lorentzian broadening function are presented to illustrate important features of quantum well laser gain spectra. From these calculations we see that the effect of a lower hole mass leads to a lower transparency current, a larger gain bandwidth for the same current level, and a larger differential gain for low threshold gain structures.

3.2 Effects of Strained InGaAs on Quantized Energy Levels

3.2.1 Strained InGaAs Subbands

The effective band gap of a strained InGaAs quantum well sandwiched between AlGaAs barriers is given by the sum of the bulk InGaAs bandgap (including strain) and the lowest quantized subband energies in the conduction and valence bands, as illustrated in Figure 3.1. This section will focus on the calculation of the band edge transition wavelength as a function of indium composition, x, and quantum well width. Increasing the indium content has two competing effects which must be taken into account when calculating the band gap. First, the effective band gap is decreased due to the incorporation of lower band gap InAs into the well. Second, increasing x also causes an increase in the effective gap due to the increased strain in the well

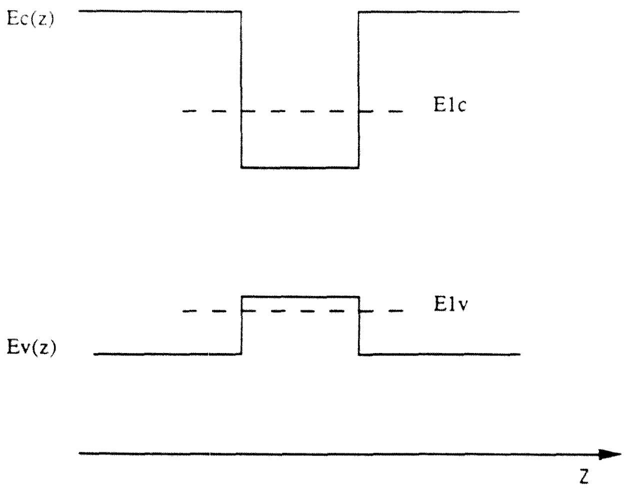

Figure 3.1: Lowest transition energy in strained InGaAs single quantum well.

[6]. In practice, due to the maximum allowable layer thickness for a given strain, the longest achievable wavelength in this material system is near $1.1\mu m$.

At the subband edge the component of k in the x-y plane, $k_{||} = 0$, and the valence and conduction band wavefunctions are decoupled and can be treated as single isolated bands [15]. The spatial dependence of the wavefunction can be written as

$$\Psi_{c,v}(r) = \chi_{c,v}(z)e^{i\mathbf{k}_{||}\mathbf{r}_{||}}u_{c,v}(\mathbf{r}) \tag{3.1}$$

where $\chi_{c,v}(z)$ is a slowly varying envelope function and $u_{c,v}(r)$ is the Bloch function periodic with the crystal lattice. The envelope function in each band then satisfies the Schrodinger equation in each of the heterostructure layers :

$$\frac{-\hbar^2}{2m^*_{c,v}}\frac{d^2}{dz^2}\chi(z) + (V(z) - E_{nc,v})\chi(z) = 0 \tag{3.2}$$

with χ and $\frac{1}{m^*}\chi'(z)$ continuous at the interfaces. The potential V(z) is equal to 0 in the well and V_0 in the barrier. The subband energies then satisfy the implicit equations

$$\sqrt{(\frac{V_0}{E_n} - 1)\frac{m^*_w}{m^*_b}} = tan(\sqrt{\frac{2m^*_w}{\hbar^2}E_n}\frac{L_z}{2}), n = 1, 3, ... \tag{3.3}$$

$$-\sqrt{(\frac{V_0}{E_n} - 1)\frac{m^*_w}{m^*_b}} = cot(\sqrt{\frac{2m^*_w}{\hbar^2}E_n}\frac{L_z}{2}), n = 2, 4, ... \tag{3.4}$$

The masses $m^*_{w,b}$ refer to bulk carrier masses corresponding to motion perpendicular to the quantum well in the well and in the barrier regions, respectively. V_0 is the barrier height and E_n is the subband energy, with the zero energy at the bulk band edge, to be determined. Compressive strain increases the bulk band gap of the well material which effectively lowers V_0. The increase in band gap is given by

$$\Delta E_g = a\epsilon_{||} \tag{3.5}$$

where a is the hydrostatic deformation potential and $\epsilon_{||}$ is the in-plane strain. The barrier potential in the conduction and valence bands are then given by

$$V_{0,c} = \Delta E_g R$$

$$V_{0,v} = \Delta E_g(1 - R)$$

with R the band offset ratio. For this ratio we use the model of reference [6]. Then the transition energy between the first subbands in the conduction and valence bands is

$$E_{11} = E_g^{bulk} + E_{strain} + E_{1c} + E_{1v} \tag{3.6}$$

and the transition wavelength is

$$\lambda = \frac{hc}{E_{11}}.$$

Figure 3.2 shows calculated band edge transition wavelengths for InGaAs quantum wells for various mole fractions and quantum well widths with GaAs barriers. The material parameters used in this calculation are taken from Reference [4] and are summarized in Table 3.1. These curves have been found to agree well with photoluminescence and TEM data [12], and are useful for estimating the indium content and quantum well width in InGaAs quantum well laser material.

3.2.2 Band Mixing in Strained InGaAs

In order to understand the effect of strain and quantization on the valence band density of states, it is necessary to consider the interactions between the bands. The dominant interaction is between the heavy and light hole bands [12,14,11,13] and is the only one considered here. In a quantum well, energies of both the heavy hole and light hole bands are quantized in the z direction, and subbands consisting of a mixture of heavy and light holes are formed. The wavefunction for the carrier in the n^{th} subband can be written as

$$\Psi_n = \sum_{h=1}^{\infty} \alpha_h \chi_h(z) |HH> + \sum_{l=1}^{\infty} \alpha_l \chi_l(z) |LH> \tag{3.7}$$

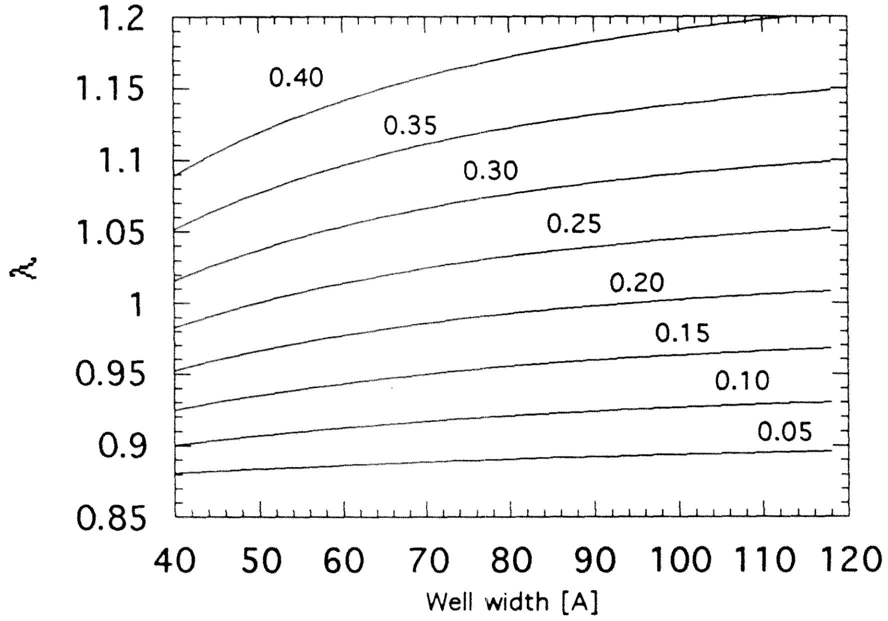

Figure 3.2: Calculated transition wavelength for a strained InGaAs single quantum well with GaAs barriers as a function of well width, for various indium molefractions.

	GaAs	**InAs**	**AlAs**
Lattice constant [A]			
a0	5.6533	6.0584	5.6605
Conduction band effective mass			
m^*c	0.0665	0.027	
Luttinger parameters			
$\gamma 1$	6.85	19.67	3.45
$\gamma 2$	2.1	8.37	0.68
$\gamma 3$	2.9	9.29	1.29
γave	2.5	9.0	0.99
Elastic Constants [* 10^{11} dyn/cm^2]			
C11	11.88	8.33	
C12	5.37	4.526	
C44	5.94	3.959	
Deformation Potentials [eV]			
Hydrostatic: av	- 8.0	- 6.0	
Shear : b	- 1.7	- 1.8	
Spin Orbit Energy [eV]			
Δ	0.34	0.38	0.28
Alloy Bulk Bandgap [eV]			
AlxGa1-xAs	$1.424 + 1.247*x$		
InxGa1-xAs	$1.424 - 1.601*x + 0.54 *x^2$		

Table 3.1: Material constants used in this chapter for calculating energy levels (from Reference [4]).

with $\chi_{h,l}(h = 1, 2, ..., l = 1, 2, ...)$ is the envelope function for the heavy (h) or light (l) hole subband evaluated at $k_{||} = 0$. The $|HH>$ and $|LH>$ Bloch parts of the wavefunctions can be written in terms of the $|J, m_j>$ basis as [11,12,14]

$$|HH> = \frac{e^{i(\frac{3\pi}{4} - \frac{3\phi}{2})}}{\sqrt{2}}|3/2, 3/2> - \frac{e^{-i(\frac{3\pi}{4} - \frac{3\phi}{2})}}{\sqrt{2}}|3/2, -3/2>$$

$$|LH> = \frac{e^{i(-\frac{\pi}{4} + \frac{\phi}{2})}}{\sqrt{2}}|3/2, -1/2> - \frac{e^{-i(-\frac{\pi}{4} + \frac{\phi}{2})}}{\sqrt{2}}|3/2, 1/2>$$

where $\phi = tan^{-1}(\frac{k_y}{k_x})$. Solving the multiband effective mass equation in the envelope function scheme has been shown to be an accurate method of calculating wavefunctions and energy levels in heterostructures for finite in-plane wavevector $k_{||}$ [15,16]. We consider the simplest model which assumes infinite barrier heights so that band edge wavefunctions and their interactions can be calculated analytically. The problem is further simplified by limiting the number of subbands to one light hole and two heavy hole bands, i.e., h = 1,2 and l = 1 in the expansion above. The omission of other bands gives less than 5% error [13] in calculating the highest valence band energy dispersion. The resulting 3X3 Hamiltonian is diagonalized as a function of $k_{||}$ to give the subband dispersion relations, and the eigenvectors quantify the amount of mixing between the bands. From these calculations we find the valence band density of states, the reduced density of states, and the polarization dependence of the matrix element for the lowest e-h1 transition.

The Luttinger Hamiltonian [7,8]describing the interactions between the light and heavy holes in strained InGaAs in the $|HH>, |LH>$ basis is given by [10,14,13]

$$H_{LK} = \begin{pmatrix} H_{hh} + S & C + iB \\ C - iB & H_{lh} - S \end{pmatrix} \tag{3.8}$$

where

$$H_{hh} = E_v - \frac{\hbar}{2m_0}[(\gamma_1 - 2\gamma_2)(i\frac{d}{dz})^2 - (\gamma_1 + \gamma_2)k_{||}^2]$$

$$H_{lh} = E_v - \frac{\hbar}{2m_0}[(\gamma_1 + 2\gamma_2)(i\frac{d}{dz})^2 - (\gamma_1 - \gamma_2)k_{||}^2]$$

$$B = \frac{\hbar}{m_0}\sqrt{3}\gamma_3 k_{||}(i\frac{d}{dz})$$

$$C = \frac{\hbar}{m_0}\frac{\sqrt{3}}{2}\gamma_{ave}$$

$$S = -b\frac{C_{11} + C_{12}}{C_{11}}\epsilon_{||}$$

The $\gamma's$ are the Luttinger parameters of the material, the C_{ij} are the elastic coefficients, and b is the shear deformation potential. At $k_{||} = 0$ the coupling terms B,C are zero and the decoupled heavy and light hole envelope functions each satisfy the single band Schrodinger equation 3.2 with effective masses

$$m_h^* = \frac{1}{\gamma_1 - 2\gamma_2}$$

$$m_l^* = \frac{1}{\gamma_1 + 2\gamma_2}$$

In the infinite well approximation, the band edge wavefunctions and energies for light and heavy holes become

$$\chi_n^{h,l}(z) = \sqrt{\frac{2}{l_z}}sin(\frac{n\pi}{l_z})$$

$$E_n^{h,l} = \frac{\hbar^2}{2m_{l,h}^*}(\frac{n\pi}{l_z})^2$$

The interactions between hh1, hh2, and lh1 are calculated using the envelope functions above and H_{LK}. For the hh1-lh1 interaction

$$c_{11} = <\chi_1^h|C + iB|\chi_1^l> = \frac{\sqrt{3}}{2}\gamma_{ave}k_{||}^2$$

and similarly for the coupling between hh2 and lh1

$$c_{21} = \frac{8}{\sqrt{3}}\frac{\gamma_3}{l_z}k_{||}$$

and the Hamiltonian on the hh1, hh2, lh1 basis is

$$H_{3X3} = \begin{pmatrix} E_{h1} - E_i & 0 & c_{11} \\ 0 & E_{h2} - E_i & c_{21} \\ c_{11}^* & c_{21}^* & E_{l1} - E_i \end{pmatrix}$$

with

$$E_{h1} = S - \frac{\hbar^2}{2m_0}((\gamma_1 - 2\gamma_2)(\frac{\pi}{l_z})^2 + (\gamma_1 + \gamma_2)k_{||}^2)$$
$$E_{h2} = S - \frac{\hbar^2}{2m_0}((\gamma_1 - 2\gamma_2)(\frac{2\pi}{l_z})^2 + (\gamma_1 + \gamma_2)k_{||}^2)$$

and

$$E_{l1} = -S - \frac{\hbar^2}{2m_0}((\gamma_1 + 2\gamma_2)(\frac{\pi}{l_z})^2 + (\gamma_1 - \gamma_2)k_{||}^2)$$

The valence band energies vs. k are then solutions of

$$(E - E_{h1})(E - E_{h2})(E - E_{l1}) - (|c_{21}|^2(E - E_{h1}) + |c_{11}|^2(E - E_{h2})) = 0 \qquad (3.9)$$

This equation has three roots $E_n(n = 1, 2, 3)$, corresponding to one of the three energy bands. The normalized wavefunction for the n^{th} (n=1,2,3) subband can be expressed in terms of our reduced basis as

$$\mathbf{F}_n = A \begin{pmatrix} -c_{11}(E_{h2} - E_n) \\ -c_{12}(E_{h1} - E_n) \\ (E_{h1} - E_n)(E_{h2} - E_n) \end{pmatrix} \qquad (3.10)$$

with the normalization constant

$$A = [|c_{11}|^2(E_{h2} - E_n)^2 + |c_{12}|^2(E_{h1} - E_n)^2 + ((E_{h1} - E_n)(E_{h2} - E_n))^2]^{-\frac{1}{2}}$$

Calculated valence band dispersion curves and the density of states of the highest band (h1), for $GaAs$ and $In_{0.2}Ga_{0.8}As$ 100 A quantum wells with infinite barriers, are shown in Figure 3.3. The strain effectively splits the energy band edges in InGaAs and reduces the coupling between the subbands compared with the GaAs case. The density of states, proportional to the slope of $\frac{1}{E(k)}$, is therefore significantly lower for the strained quantum well. This calculation estimates the in-plane hole effective mass $m_h = 0.08m_0$ for InGaAs, a significant reduction compared with $m_h = 0.45m_0$ for bulk GaAs. The effective hole mass in strained InGaAs has been measured, with $m_h = 0.14m_0$ by Jones et al. [17].

We can also calculate the matrix element once the expansion coefficients of the electronic wavefunction in our reduced basis are known. For the lowest transition, the lowest conduction state e1 to the highest valence band state h1, and a polarization unit vector ϵ, the matrix element is given by

$$\mathbf{M} = < h_1|e\epsilon\mathbf{r}|e1 >$$

The Bloch function in the conduction band has atomic orbital S symmetry [7,9] and we write the wavefunction for electrons in an infinite well as

$$\Psi_c = \sqrt{\frac{2}{l_z}} sin(\frac{n\pi}{l_z})|S >$$

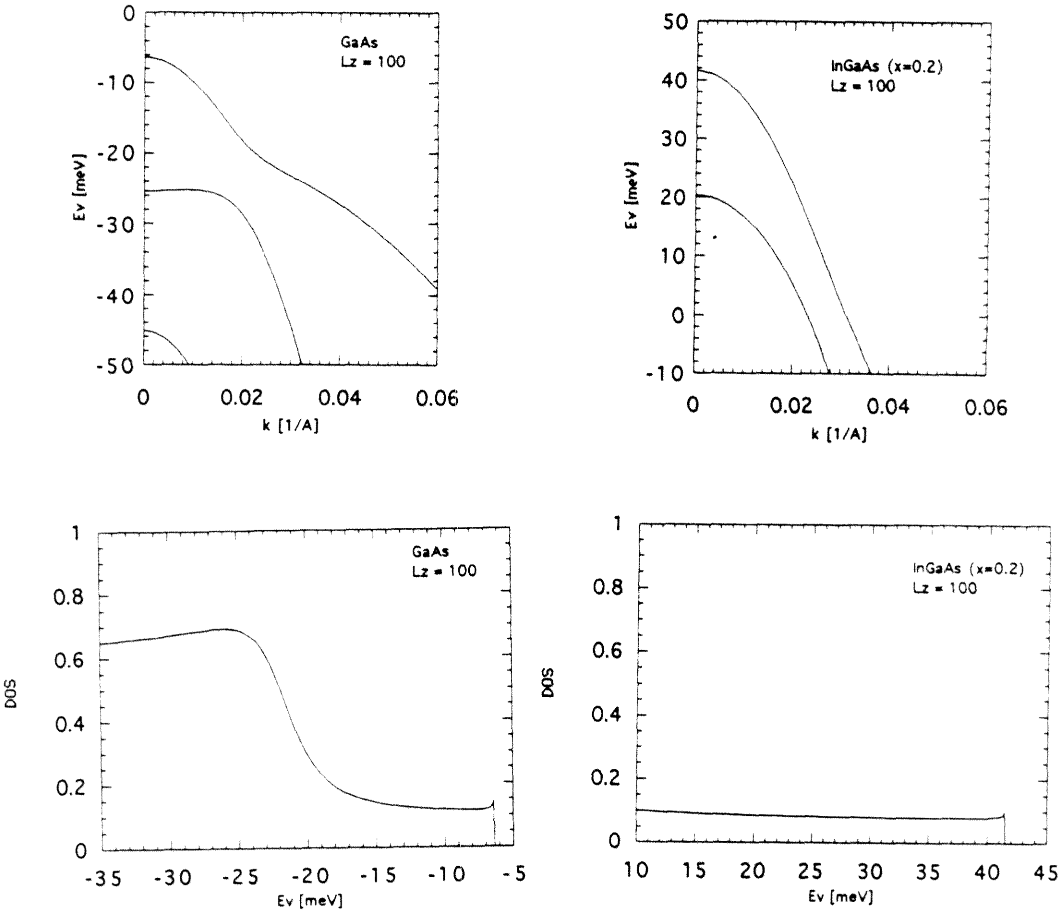

Figure 3.3: a)Calculated E(k) and for a 100 A single quantum well with infinite barriers, including coupling between two heavy hole bands and one light hole band, for GaAs and $In_{0.2}Ga_{0.8}As$. b) The density of states (DOS) normalized by a free electron 2D DOS ,$\rho_0 = \frac{m_0}{\pi\hbar^2}$, for the highest hole band for the two structures.

For TE modes, the polarization vector is in the plane of the well, i.e., $\epsilon = \mathbf{x}$, and the matrix element, averaged over azimuthal angle ϕ, can be found from the components of $\mathbf{F_n} = (F_{n1}, F_{n2}, F_{n3})$. After transforming the valence band wavefunctions back from the $|J, m_j>$ basis to the atomic p orbital functions $|X>, |Y>, |Z>$ we find for the lowest order transition e1-h1

$$|M|^2_{TE} = \frac{|<Z|ez|S>|^2}{4}(F_{11}^2 + \frac{F_{13}^2}{3})$$

.

For TM modes the polarization is perpendicular to the well, $\epsilon = \mathbf{z}$, and the matrix element for the e1-h1 transition becomes

$$|M|^2_{TM} = |<Z|ez|S>|^2 \frac{F_{13}^2}{3}$$

The TE matrix element is larger than the TM matrix element in both GaAs and compressively strained InGaAs, and, therefore, most important for gain. A plot of the calculated TE matrix element is shown in Figure 3.4 as a function of in-plane wavevector. The larger TE matrix element for the InGaAs is a result of the lowered amount of mixing and, hence, larger heavy hole character of the highest valence band in the strained material.

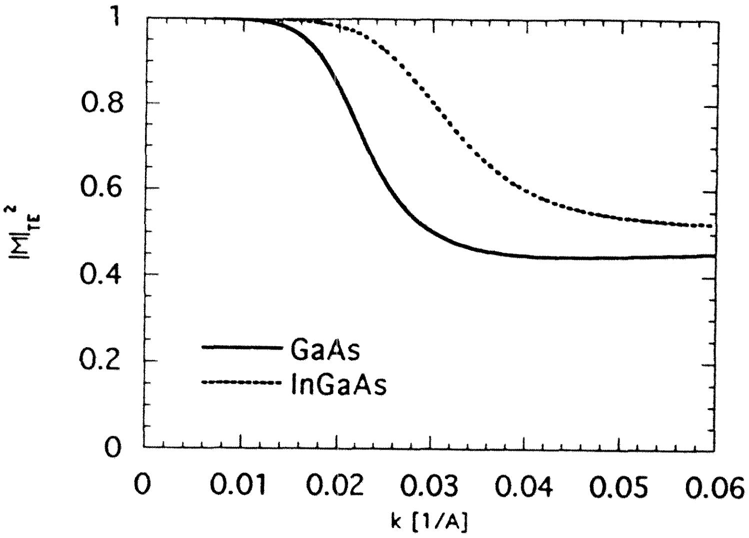

Figure 3.4: Calculated TE matrix element for the e1-h1 transition for the same structures in Figure 3.3. The matrix element is normalized to its value at $k_{||} = 0$.

3.3 Spectral Gain

3.3.1 Absorption and Transition Rates

The electric field of a plane wave, polarized along **z** (TE), and traveling along **y** in an amplifying medium, can be described by exponential gain and loss coefficients γ and α [18],

$$E_z = E_0 e^{(\gamma-\alpha)y} e^{i(ky-\omega t)} + cc. \tag{3.11}$$

The optical loss, in cm^{-1}, due to absorption of a photon which excites an electron from state 1 to state 2, can be calculated in terms of B_{12} and the using Fermi's Golden Rule. The Einstein coefficients A_{21}, B_{21}, and B_{12} are the spontaneous and stimulated transition rates between energy levels 1 and 2. To derive α, we consider the net rate of upward transitions [s^{-1}] due to a photon density $P(E_{21})$ of frequency $\omega_{21} = E_2 - E_1$ is

$$r_{12} = B_{12}(f_1 - f_2)P(E_{21}) \tag{3.12}$$

where $f_{1,2}$ are the fermi occupation factors for levels 1 and 2 given by

$$f_{1,2} = \frac{1}{e^{\frac{(E_{1,2}-E_f)}{kT}} + 1} \tag{3.13}$$

where we have used $B_{12} = B_{21}$. Now it remains to relate the net rate of upward transitions [s^{-1}] to the absorption coefficient [cm^{-1}]. The net absorption rate is the loss coefficient, α, multiplied by the photon flux. But the photon flux is just the photon density, $P(E_{21})$, multiplied by the group velocity, v_g. Thus, we have

$$\alpha = \frac{r_{21}}{P(E_{21})v_g} \tag{3.14}$$

or, substituting equation 3.12 into 3.14,

$$\alpha = \frac{B_{12}}{v_g}(f_1 - f_2) \tag{3.15}$$

B_{12} can be calculated using Fermi's Golden Rule for the transition from one state to a group of final states, ρ_f, under the influence of an electromagnetic field. For a time-dependent harmonic perturbation, the transition rate is given by

$$B_{12} = \frac{2\pi}{\hbar}| < \Psi_f|H^I|\Psi_i > |^2 \rho_f(E_{final} = E_{initial} + \hbar\omega) \tag{3.16}$$

where $H^I = \mathbf{A.p}$ is the interaction Hamiltonian causing the transition. For a plane wave with a vector potential $\mathbf{A}$, we can find B_{12} in terms of the matrix element $|\mathbf{M}|^2 = <\mathbf{p}>$. If the plane wave is polarized along $\mathbf{z}$ and propagating along $\mathbf{y}$, the vector potential $\mathbf{A}$ can be written as $\mathbf{A} = \mathbf{e}_z[A_0 e^{i(ky-\omega t)} + A_0^* e^{-i(ky-\omega t)}]$.

The initial and final states are

$$\Psi_{i,f} = \phi_{i,f}(x, y, z)e^{-\omega_{i,f}t}. \tag{3.17}$$

Writing the matrix element between the initial and final states with the momentum operator as

$$|M|^2 = | < \phi_f|p_z|\phi_i > |^2 \tag{3.18}$$

we obtain

$$B_{12} = (\frac{2\pi}{\hbar})(\frac{q^2}{m_0^2})(\frac{2\hbar\omega}{\epsilon})(\frac{1}{4\omega^2})|M|^2\rho_{final}. \tag{3.19}$$

3.3.2 K - Selection Rule

When calculating the absorption due to valence-conduction band transitions, we consider only the case where the crystal momentum, $\mathbf{k}$, of the electron in the initial state is equal to that of the electron in the final state; that is $\mathbf{k}_c = \mathbf{k}_v$. This is true since k must be conserved in the overall process, and because the momentum of the emitted photon is much less than the momentum of the electron in the conduction and valence bands. This puts a restriction on the density of final conduction band states, ρ_f, included in the transition rate in equation 3.19. To find the rate of absorption in the semiconductor, we relate the density of allowed transitions at the photon energy E_{ph} to the density of states in the conduction and valence bands. The photon energy is given in terms of the band gap energy, E_g, the conduction band energy, E_c, and valence band energy, E_v, as

$$E_{ph} = E_g + E_c + E_v. \tag{3.20}$$

A change in E_{ph}, therefore, corresponds to a change in E_c and E_v

$$dE_{ph} = dE_c + dE_v. \tag{3.21}$$

Using the density of states for a two dimensional system in the conduction and valence bands

$$\rho_{c,v}(E_{c,v}) = \frac{k_{c,v}}{\pi}\frac{dk_{c,v}}{dE} \tag{3.22}$$

we find that the density of allowed transitions, or the reduced density of states, is given by

$$\frac{1}{\rho_r(E_{ph})} = \frac{1}{\rho_c(E_c)} + \frac{1}{\rho_v(E_v)}. \tag{3.23}$$

In calculating the density of states in the conduction and valence bands, a factor of two is included to account for two spin states at each energy. However, since spin must be conserved in the transition, the number of allowed transitions above must be calculated using 1/2 the total density of states in the valence and conduction bands.

3.3.3 Parabolic Uncoupled Bands

For parabolic subbands with effective masses $m^*_{c,v}$, the energy of the electron in the conducton band, E_c, and hole in the valence band, E_v, is

$$E_{c,v}(k) = E_n + \frac{\hbar^2 k^2}{2m^*_{c,v}} \tag{3.24}$$

where E_n is the energy of the nth subband and $\frac{\hbar^2 k^2}{2m^*_{c,v}}$ is the kinetic energy. Thus the density of states for each subband for a 2D system with parabolic bands is

$$\rho_{c,v} = \frac{m^*_{c,v}}{\pi \hbar^2}. \tag{3.25}$$

This allows us to write

$$\rho_r = \frac{1}{2}\frac{m^*_r}{\pi \hbar^2} \tag{3.26}$$

where

$$\frac{1}{m^*_r} = \frac{1}{m^*_c} + \frac{1}{m^*_v} \tag{3.27}$$

3.3.4 Gain Equations

Now that we have an expression for the density of transitions and for B_{12}, we can write the equation for gain, γ . Substituting equation 3.19 into the expression 3.15 for α and recalling that $\gamma = -\alpha$, we obtain

$$\gamma(E) = \frac{hq^2}{2m^2 \epsilon E v_g} |M|^2 \rho_r (f_c + f_v - 1) \tag{3.28}$$

Thus we have a general expression for gain due to stimulated transitions in a semiconductor, characterized by a conduction and valence band density of states, under k-selection rules. In this expression, f_c is the probability to find an electron in the conduction band and f_v is the probability of finding a hole in the valence band at the transition energy E. We have assumed quasi-equilibrium in the bands; that is, the occupation in the valence and conduction bands can be described by quasi Fermi energies E_{fc}, E_{fv} and

$$f_{c,v} = \frac{1}{e^{\frac{(E_{c,v} - E_{fc,v})}{kT}} + 1} \tag{3.29}$$

The factor $f_c(E_c) + f_v(E_v) - 1$ represents the population inversion between the energy E_c in the conduction band and E_v in the valence band. Thus the dependence of the gain on carrier density is implied through the fermi energies. For a given carrier injection, the fermi energies can be calculated via

$$n = \int_{E_c=0}^{\infty} \rho_c(E_c) f_c dE_c. \tag{3.30}$$

The valence band fermi level, E_{fv}, can be found similarly assuming charge neutrality $n = p$. For a constant density of states, this integral can be performed exactly; however, in general it must be solved numerically or by approximation methods.

By inspection of equation 3.28, we see that the low energy spectrum is dominated by the shape of $\rho_r(E)$, whereas the high energy side is cut off by the Fermi functions. Therefore, for a step-like density of states, the gain will level off to a peak value, γ_0, for energies with an inversion factor near unity, and fall off exponentially at energies above the Fermi levels. The gain is equal to zero for a photon energy

$$E_{ph}^{tr} = E_{fc} + E_{fv} + E_g \tag{3.31}$$

This is the transparency condition. For energies greater than E_{ph}^{tr} the material is absorbing, and for lower energies (above the band gap) the material is amplifying.

3.3.5 Transition Broadening

The expression for gain in equation 3.28 assumes perfectly defined transitions as well as a perfect two dimensional density of states. The model thus predicts sharp features in the gain spectra due to the onset of higher subband transitions in the step-like reduced density of states. In actual gain spectra, the sharp structure is smoothed out due to carrier collisions and quantum well roughness. To model the uncertainty in subband energy, each transition is given a lineshape $B(E, E_0)$. The contributions to the gain at energy E_0 will then include all other transitions weighted by the lineshape function. Mathematically, the gain is expressed as a convolution integral

$$g(E_0) = \int_{E=0}^{\infty} \gamma(E) B(E, E_0) dE \tag{3.32}$$

For a collision broadened two-level system with a collision time T_2, the broadening function is given by a Lorentzian centered at E,

$$B(E, E_0) = \frac{T_2}{\pi\hbar(\frac{(E_0 - E)T_2}{\hbar})^2 + 1}.$$

In addition to smoothing out sharp features, the broadening also decreases the peak gain. Although the energy tails in the Lorentzian have been shown to be too wide to quantitatively explain certain features of the gain spectra [6], we will use it to show some of the main trends in the spectral gain curves.

3.4 Calculated Gain Spectra

As we have seen in Section 2, the main effects of strain on laser performance are a shift in the bandgap and a decreased valence band effective mass. This latter effect can be incorporated into the parabolic band approximation by simply assuming a decreased effective hole mass in the InGaAs. To illustrate the effect of strain on laser performance, we will use equations 3.28 and 3.32 to calculate the gain for two different cases: the GaAs case and the case of InGaAs where the electron mass is the same as GaAS but the hole mass is decreased. In Section 2.2 the valence band effective mass was calculated to be 0.08 m_0 using the envelope function formalism. This is fairly close to the GaAs electron mass of 0.067 m_0 which we will use here to illustrate differences between GaAs and strained InGaAs gain.

3.4.1 Carrier Injection Efficiency

The lower bandgap of InGaAs, compared with GaAs, in the quantum well will increase the barrier height for both electrons and holes for a given $Al_xGa_{1-x}As$ barrier material. As the height increases, fewer carriers will populate the $Al_xGa_{1-x}As$ for a fixed carrier density in the quantum well [5,23]. Since the barrier region is much thicker ($d_{barrier} > 1000\mathring{A}$) than the well, the number of "wasted" carriers in the barrier can be significant. We define the electron injection efficiency as

$$\eta_e = \frac{n_{qw}}{n_{qw} + n_{barrier}} \tag{3.33}$$

for n_{qw}, $n_{barrier}$ electrons in the well and barrier regions respectively. The efficiency can be calculated by integrating the conduction band density of states given by

$$\rho_{c,qw}(E_c) = \sum_{n=1}^{n_c} \frac{m_c^*}{\pi\hbar^2} H(E_c - E_{nc}) \tag{3.34}$$

for $E_c < V_c$ and

$$\rho_{c,qw}(E_c) = l_z \frac{\sqrt{2}}{\pi^2} \frac{m_c^{*\frac{3}{2}}}{\hbar^3} \sqrt{E_c - V_c} \tag{3.35}$$

for $E_c > V_c$.

In the barrier material ($E_c > V_c$), the density of states is written as

$$\rho_{c,barrier}(E_c) = d_{barrier} \frac{\sqrt{2}}{\pi^2} \frac{m_c^{*\frac{3}{2}}}{\hbar^3} \sqrt{E_c - V_c} \tag{3.36}$$

The summation in ρ_{qw} is over all the bound states in the well. The valence band density of states is similar with the summation including all bound light and heavy hole states.

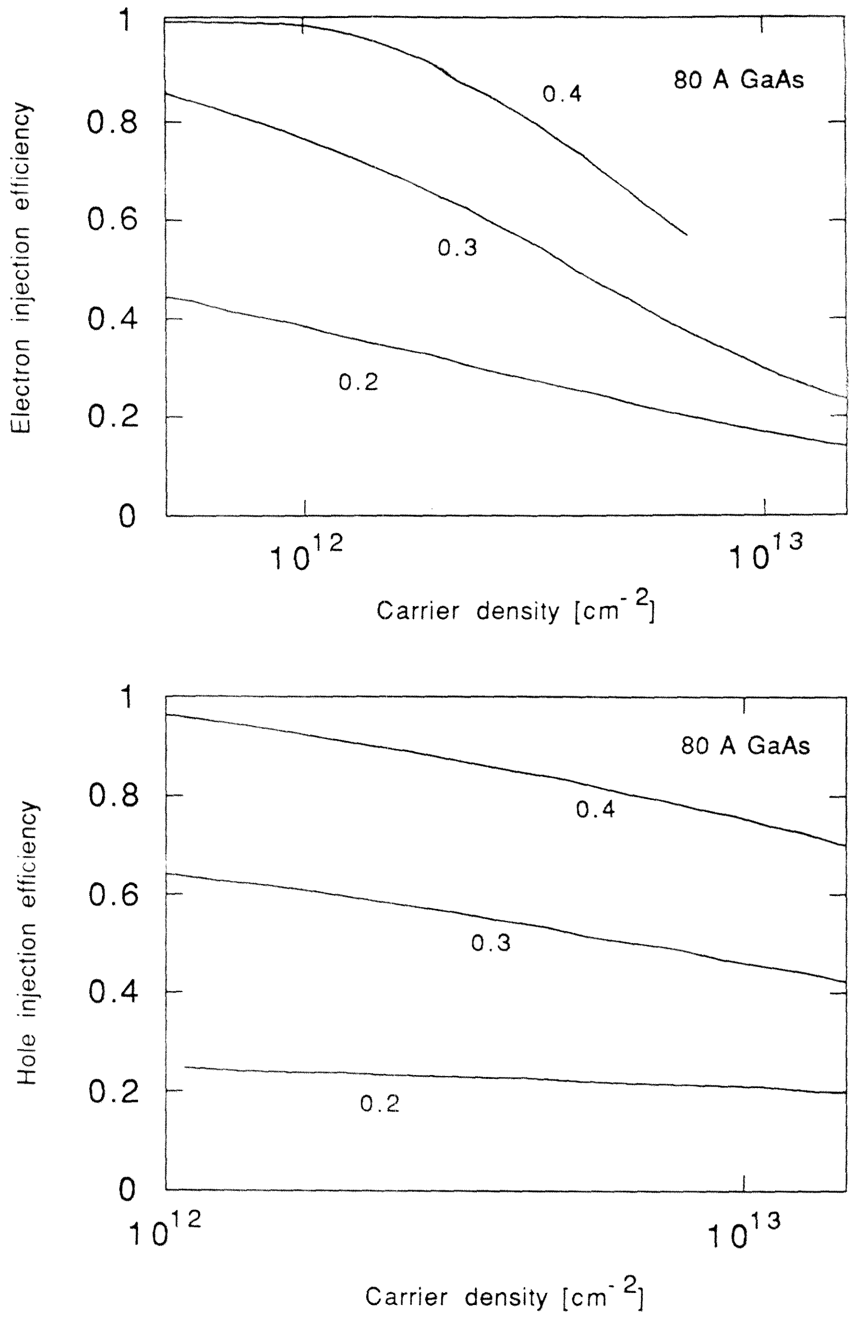

Figure 3.5: Calculated electron and hole injection efficiency for an $80\mathring{A}GaAs$ quantum well as a function of total carrier density for various aluminum concentrations in the barrier.

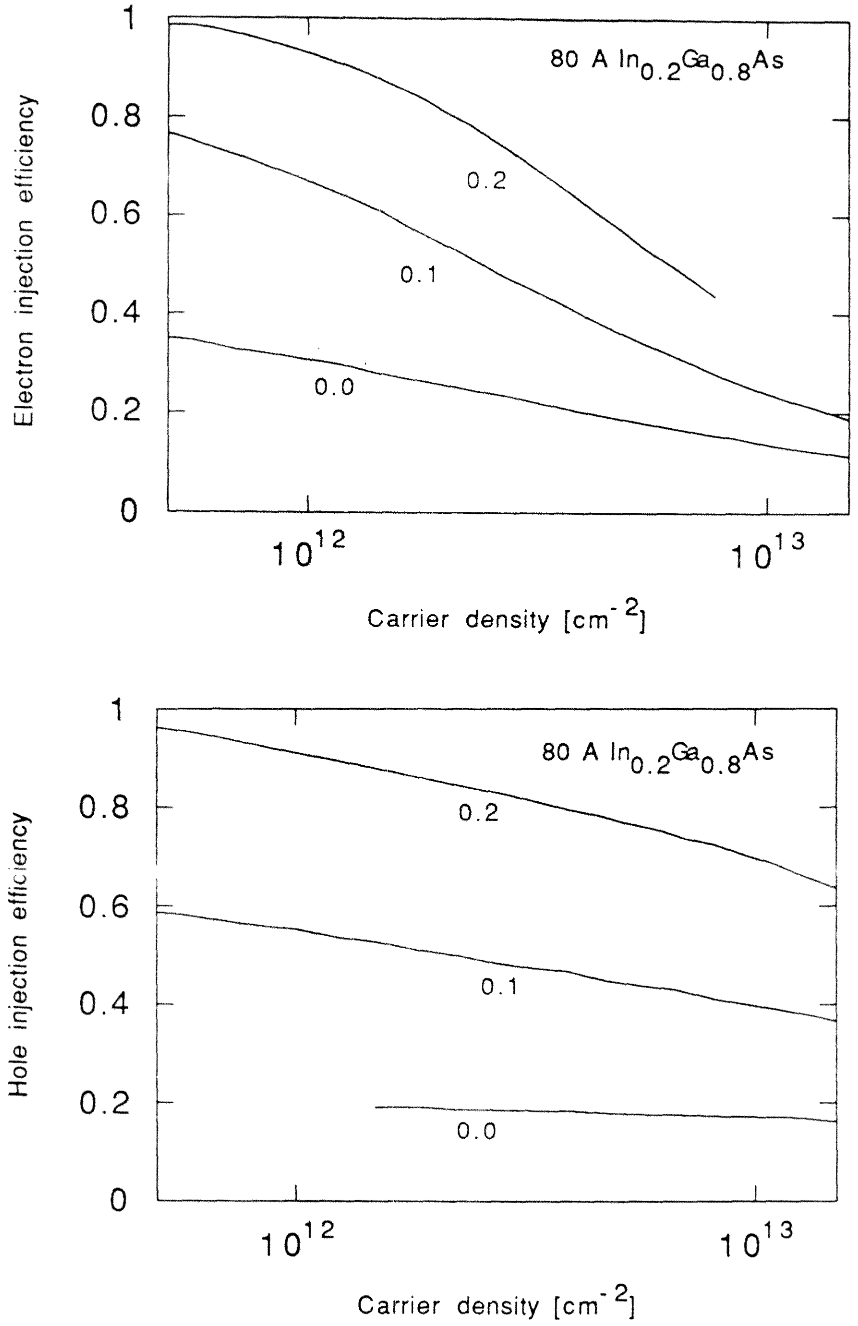

Figure 3.6: Calculated electron and hole injection efficiency for an $80\AA In_{0.2}Ga_{0.8}As$ quantum well as a function of total carrier density for various aluminum concentrations in the barrier.

Figures 3.5 and 3.6 show the calculated efficiency of injected electrons and holes for $80\AA GaAs$ and $In_{0.2}Ga_{0.8}As$ quantum wells, respectively, with various barrier aluminum concentrations. For the same aluminum content in the barrier, the efficiency can be as much as 5X larger for the InGaAs case.

3.4.2 Calculated Gain

The gain is calculated for the n=1 and n=2 transitions using a lorentzian convolution with a relaxation time $T_2 = 0.1$ ps. Figure 3.7 shows calculated gain spectra at two different injection levels, for equal electron and hole masses as well as for the GaAs case where $m_v^* = 7m_c^*$. In both cases the peak gain shifts to higher energies with higher pumping. At a certain level, the gain at the n = 2 level becomes larger than the gain at the n = 1 state. For the same low level injection, the equal mass case gives a larger peak gain. The maximum available gain from a given subband, however, is larger in the nonequal case due to the larger reduced density of states. This condition is reached at high current levels. Another interesting feature is that the bandwidth of positive gain is significantly larger for the equal mass case which is useful for tunability purposes.

The transparency current is also lowered by lowering the valence band effective mass. Figure 3.8 shows the transparency current as a function of the ratio of valence band effective mass to conduction band effective mass. Figure 3.9 shows the peak gain vs. current in a simple model [12] for the two cases. The differential gain is larger for low currents but levels off and saturates easily for the low hole mass.

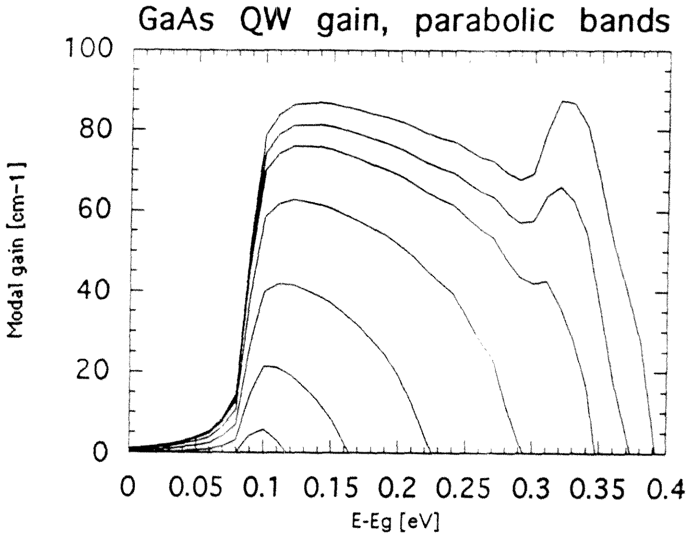

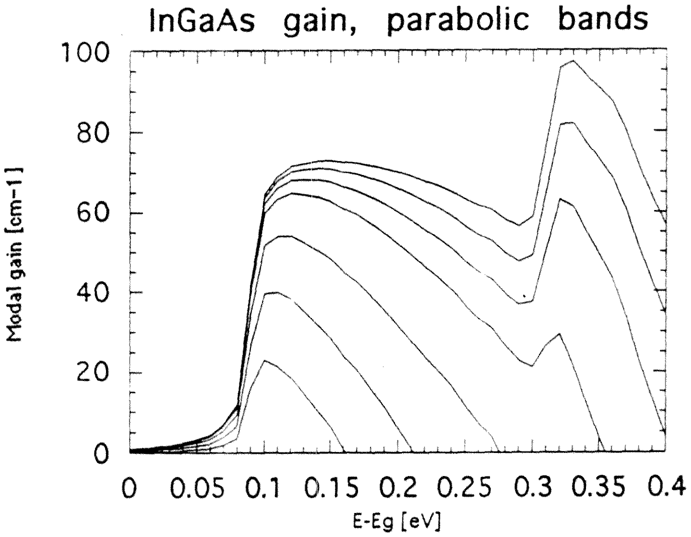

Figure 3.7: Calculated gain spectra for a) $m_v = 0.45$ (GaAs) b) $m_v = 0.07$ for carrier densities from 10^{12} to 10^{13}.

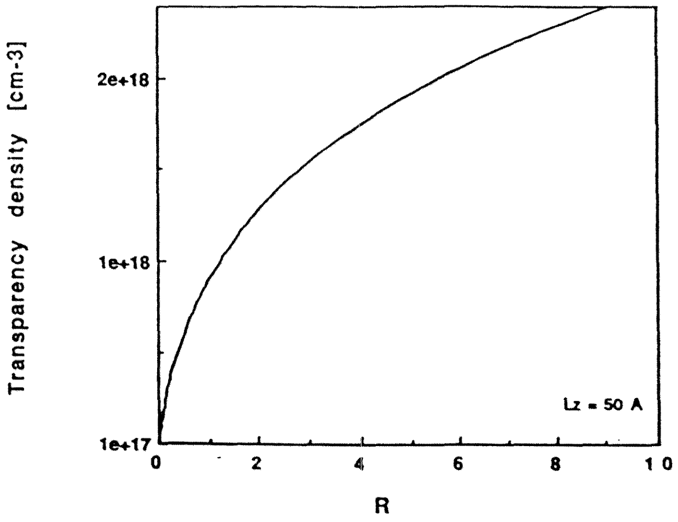

Figure 3.8: Transparency carrier density vs. valence to conduction band mass ratio R=Mv/Mc.

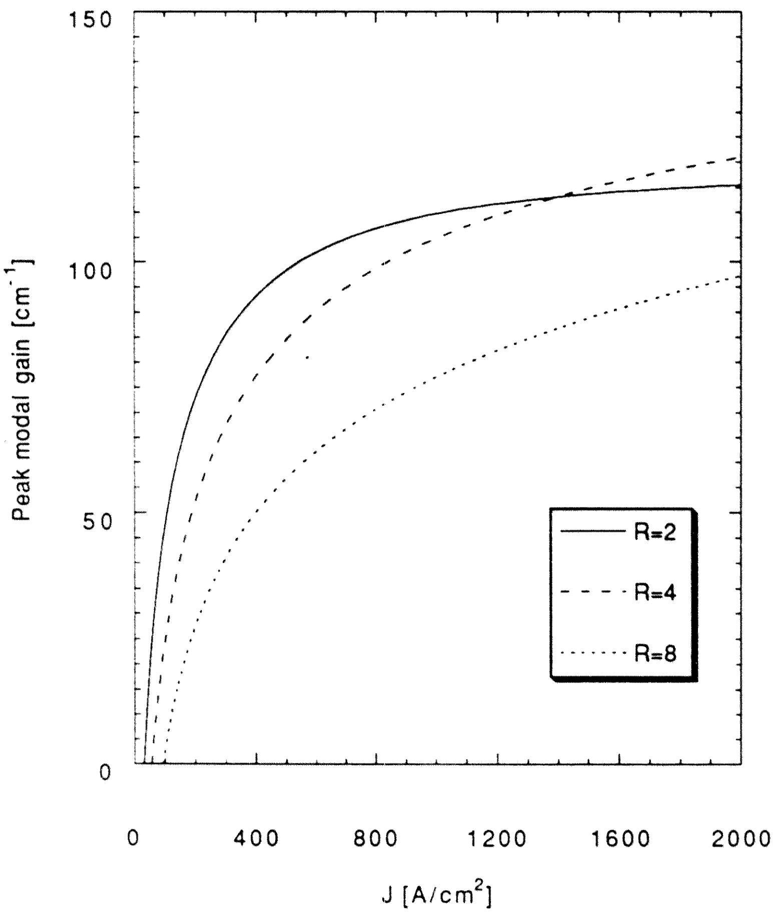

Figure 3.9: Calculated peak gain vs. current for various hole masses.

3.5 Threshold current equations

Once we have an expression for the gain in the material for a given current injection, we can use the laser oscillation condition to find the threshold current. The conditon for laser oscillation is that the gain equals the cavity losses, or

$$\Gamma g_{th} = \alpha_i + \frac{1}{L} log \frac{1}{R} \tag{3.37}$$

where

$$R = \sqrt{R_1 R_2}$$

α_i is the internal loss, L is the cavity length, and $R_{1,2}$ are the mirror reflectivites. Γ is the optical confinement factor and can be calculated for a given structure by

$$\Gamma = \frac{\int_{\frac{-L_z}{2}}^{\frac{L_z}{2}} |E_0|^2 dz}{\int_{-\infty}^{\infty} |E_0|^2 dz}. \tag{3.38}$$

and L_z is the active region width. For very thin active regions, which is certainly the case for a single quantum well, the optical field is approximately constant in the overlap integral and thus the confinement is given by

$$\Gamma = \frac{L_z}{W_{mode}}$$

where W_{mode} is the width of the optical mode.

The internal losses include the optical losses due to waveguide imperfections, free carrier absorption, and inter-valence band absorption all grouped together in a distributed loss constant. The loss term can be measured, together with the internal quantum efficiency η_i, by measuring the external quantum efficiency for various cavity lengths

$$\frac{1}{\eta_d} = \frac{1}{\eta_i}(\frac{\alpha_i L}{log\frac{1}{R}} + 1) \tag{3.39}$$

3.5.1 Threshold Current

A simple, but useful, expression for the threshold current can be obtained by linearizing the gain about the transparency carrier density. Let

$$g_{th} = g'(N - N_{tr}) \tag{3.40}$$

where g_{th} is the threshold gain, N is the carrier density, N_{tr} is the transparency carrier density, and $g' = \frac{dg}{dn}$ is a constant. To translate the carrier density to a current density, it is customary to introduce a radiative recombination constant τ :

$$J = \frac{eN}{\tau}[\frac{A}{cm^2}]. \tag{3.41}$$

This gives an explicit expression for the threshold current

$$I_{th} = \frac{eW}{\tau}(N_{tr}L + \frac{d}{g'_m}(\alpha_i L + \log\frac{1}{R})) \tag{3.42}$$

where

$$g'_m = \Gamma g'$$

and d is the active region thickness, and W the width of the device.

We have an expression for the threshold current in terms of measurable parameters. We use this equation to experimentally compare laser structures, and to optimize cavity lengths and mirror reflectivity for low threshold. The above expression will be used in the next chapter to analyze our strained layer lasers. It is important to keep in mind that we have linearized the gain to obtain this result. This is especially important in quantum well lasers as the gain becomes sublinear at reasonable carrier levels.

3.6 Conclusions

The heavy hole density of states in GaAs quantum wells is largely due to interactions with light hole bands. This valence band mixing is reduced in InGaAs quantum wells due to the strain induced splitting of the heavy and light hole energy levels. The lowest order transition, e1-h1, will thus retain a heavy hole character even as the wavevector k increases from k=0. More importantly, however, the valence band heavy hole mass is dramatically reduced from an average of $0.45m_0$ to $0.08m_0$ close to that of an electron in the conduction band. This in turn should lead to a lower transparency current, a larger gain bandwidth, and lower threshold current in strained layer quantum well lasers.

References

[1] E. Yablonovich and E.O. Kane, *J. Lightwave Tech.* **LT-4**, 504 (1986)

[2] A.R. Adams, *Electron. Lett.* **22**, 249 (1986)

[3] I. Suemune, L.A. Coldren, M. Yamanishi, and Y. Kan, *Appl. Phys. Lett.* **53**, 1378 (1988)

[4] Landolt-Bornstein, *Numerical Data and Function Relationships in Science and Technology* **17 a-b**, Springer, New York (1982)

[5] R.M. Kolbas, N.G. Anderson, W.D. Laidig, Y. Sin, Y.C. Lo, K.Y. Hsieh, and Y.J. Yang, *IEEE J. Quant. Electr.* **24**, 1605 (1988)

[6] C. Van de Walle, *Mat. Res. Soc. Symp.*, Boston (1987)

[7] J.M. Luttinger and W. Kohn, *Phys. Rev.* **97**, 869 (1955)

[8] J.M. Luttinger, *Phys. Rev. B* **102**, 1030 (1956)

[9] E.O. Kane, *J. Phys. Chem. Solids.* **1**, 249 (1957)

[10] G.E. Pikus and G.L. Bir, *Sov. Phys. Solid State* **1**, 1502 (1960)

[11] D.A. Broido and L.J. Sham, *Phys. Rev. B*, **31**, 888 (1985)

[12] A. Twardowski and C. Herman, *Phys. Rev. B* **35**, 8144 (1987)

[13] E. P. O'Reilly, Semicond. Sci. Technol. **4**, 127 (1989)

[14] D. Ahn and S. Chuang, *IEEE J. Quant. Electr.* , **24**, 2400 (1988)

[15] G. Bastard, *Wave Mechanics Applied to Semiconductor Heterostructures*, Halstead Press (1988)

[16] M. Altarelli, *Heterojunctions and Semiconductor Superlattices*, ed. G. Allen, G. Bastard, N. Boccara, M. Lanoo, and M. Voos (Springer, Berlin), 12 (1986)

[17] E.D. Jones, H. Ackermann, J.E. Shirber, T.J. Drummond, L.R. Dawson, and T.J. Fritz, *Solid St. Comm.* **55**, 525 (1985)

[18] A.Yariv, *Optical Electronics* 4^{th} edition, Saunders Publishing (1991)

[19] H. Casey and M.B. Panish, *Heterostructure Lasers*, Academic Press (1978)

[20] R.H. Yan, S. Corzine, L. Coldren, and I. Suemune, *IEEE J. Quant. Electr.* **26**, 213 (1991)

[21] M. Asada, A. Kameyama, and Y. Suematsu, *IEEE J. Quant. Electr.* **20**, 745 (1984)

[22] J. Nagle, M. Hersee, T. Weil, and C. Weisbuch, *Appl. Phys. Lett.* **49**, 719 (1985)

[23] H. Hirayama, Y. Miyake, and M. Asada, *IEEE J. Quant. Electr.* **28**, 68 (1992)

[24] S.R. Chinn, P. Zory, and A.R. Reisinger, *IEEE J. Quant. Electr.* **24**, 2191 (1988)

[25] K. Lau, S. Xin, W. Wang, N. Bar-Chaim, and M. Mittelstein, *Appl. Phys. Lett.* **55**, 1173 (1989)

[26] J.E. Schirber, I.J. Fritz, and L.R. Dawson, *Appl. Phys. Lett.* **46**, 187 (1985)

Chapter 4

InGaAs Quantum Well Laser Performance

4.1 Introduction

This chapter will describe the structure, fabrication, and possible future improvements of broad area and buried heterostructure InGaAs lasers [11,2].

It is interesting to investigate InGaAs lasers for several reasons. First, the small band gap allows lasing at longer wavelengths than GaAs; reliable operation has been shown out to $1.1\mu m$ [6]. It is of particular interest to the communications industry to have high power sources at 980 nm to efficiently pump Er^+ doped fiber amplifiers. Second, as we have seen in the previous chapter, InGaAs exhibits a larger gain than GaAs, yielding lower transparency currents and a potential for lower threshold currents. Third, the ability to fabricate deeper wells in InGaAs allows less leakage of the carriers to the confining layers. Finally, the narrower band gap of InGaAs allows us to use a narrower band gap confining region. This leads to a larger available refractive index step, and hence larger confinement of the optical mode for a larger modal gain.

4.2 Structure and Growth

The laser consists of an InGaAs quantum well active region surrounded by higher band gap, and therefore lower refractive index, GaAs and AlGaAs. The larger band gap confines the carriers to the quantum well, and the lower index provides a waveguide for the optical mode.

The epitaxial layers as shown in figure 4.1 consist of the following: a 1 μm silicon doped n-$GaAs$ buffer layer, a 1.5 μm n-$Al_{0.5}Ga_{0.5}As$ cladding layer, an 0.2 μm n-$Al_xGa_{1-x}As$ graded confinement region with x ramped parabolically from 0.5 to 0.2, a 4 nm $GaAs$ spacer, and the 5 nm $In_yGa_{1-y}As$ quantum well. The beryllium p-doped upper half of the structure is the mirror image of the n - side except for the p^+ contact layer. This layer was doped as high as possible, 2 x10 ^{19} cm^{-3}, to minimize the contact resistance. The $Al_xGa_{1-x}As$ regions provide transverse optical mode confinement as well as electronic barriers for efficient current collection. The substrate was (100) GaAs tilted 4° towards (111) A. This choice was made since we have found growth conditions to be more tolerant on this substrate type [4]. Apart from the active quantum well region, the device structure is identical to optimized GaAs quantum well lasers [7] grown in our laboratory. The substrate temperature was

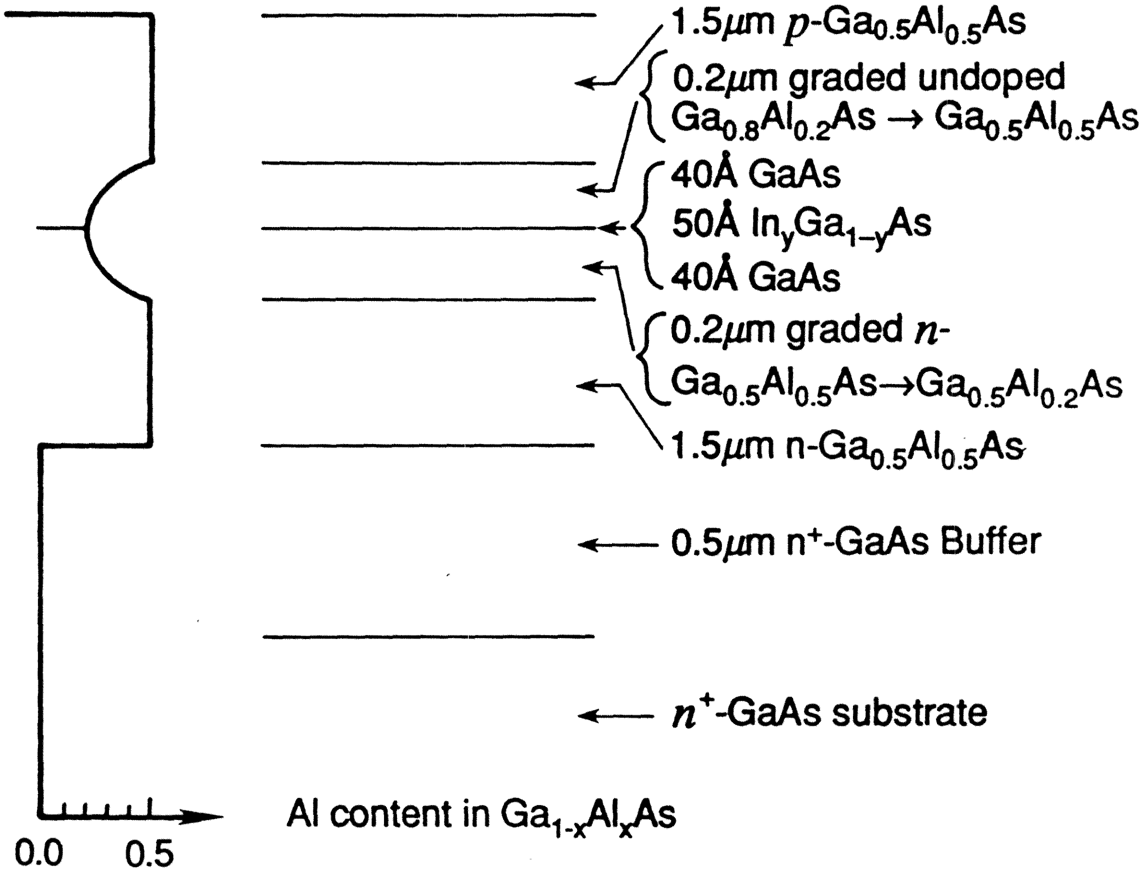

Figure 4.1: The epitaxial layer structure in the InGaAs quantum well lasers.

held at $600°C$ for the GaAs buffer and cap layers, $720°C$ in the cladding and graded $Al_xGa_{1-x}As$ regions, and ramped down to about $620°C$ for the InGaAs quantum well, where the temperatures quoted are pyrometer readings. To minimize incorporating impurities into the material, the growth is continuous throughout with no growth interruption; that is, the substrate temperature is ramped down, and then up again during the GaAs spacer growth. To quickly ramp the substrate temperature, the substrate was mounted to a direct heating holder [8]. It should be noted that the structure uses a parabolically graded confinement region. The reason for this is actually more historical than for device optimization. It has been shown theoretically [9,5] that a linearly graded profile is a better current confining structure over a wide range of threshold gains.

4.3 Broad Area Single Quantum Well Devices

After the growth, to get an estimate of the indium content and quantum well width, room temperature optical absorption of the material was measured. The absorption edge was at 1050 nm, which correponds to a 50 - 60 Ångstrom well width containing 35% indium. To test the MBE material quality, we fabricate broad area lasers with $100\mu m$ wide stripes. This consists of evaporating Cr/Au stripes on top of the material, thinning the wafer to 125 μm, depositing AuGe/Au on the back side, and annealing at 360 $°C$ for 30 seconds. Lasers of various lengths are then cleaved and light vs. current is measured. We use 200 ns current pulses at 10 kHz repetition rate to avoid heating effects. The lasing wavelength of long devices is 990 nm. Threshold current density vs. 1/L for this material is shown in 4.2. From these measurements we see that for cavity lengths greater than $400\mu m, or (J_{th} < 300\frac{A}{cm^2})$,the threshold current is linear with 1/L. For these lasers we find a good fit to the data to be

$$J_{th} = 50[\frac{A}{cm^2}] + \frac{10[\frac{A}{cm}]}{L[cm]}. \tag{4.1}$$

The lowest threshold current density measured was $J_{th} = 114\frac{A}{cm^2}$ for a $1540\mu m$ long cavity. These threshold current densities were the lowest results published, nearly 50% less than the previous best material grown by MOCVD, a factor of 5 lower than the best MBE material, and only slightly higher than the best GaAs quantum well laser material [2]. The internal loss of this structure was found to be 9 cm^{-1} with an internal quantum efficiency $\eta_i = 0.6$. Using this, we estimate a transparency current density in the material of $J_{tr} = 20-25\frac{A}{cm^2}$. Recent progress has been made by Choi et al. [5] using OMVPE, and Williams [6] using MBE, both using a structure with higher optical mode confinement, they have been able to obtain threshold current densities in InGaAs below that of the best GaAs material. They measure a transparency density of 25 $\frac{A}{cm^2}$, similar to our result. Transparency densities of the best GaAs lasers [7] are found to be nearly twice this value at $J_{tr}^{GaAs} = 50\frac{A}{cm^2}$.

4.4 Multiple Quantum Well Lasers

If the number of quantum wells is increased to N, we can still use the linearized threshold equations from chapter 2. Now, however, the confinement factor, Γ, is N

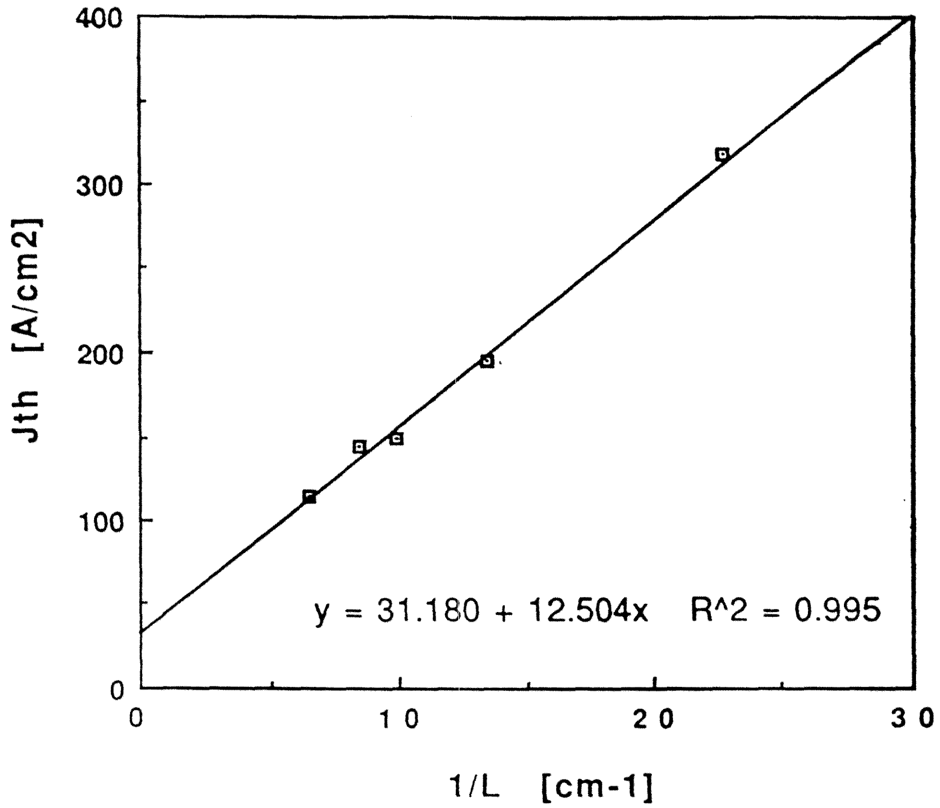

Figure 4.2: Threshold current density vs. 1/L for broad area InGaAs SWQ lasers.

times larger, and the transparency current is increased by the same factor. Also, for the same current injection, the carrier density in each well is lower by a factor N, resulting in lower quasi fermi energies and less population of confining region states. Neglecting the population of confining region states, the modal gain for the laser with N wells, compared with the single well, at a given current injection can be written as [16]

$$\frac{g_m^N}{g_m^{N=1}} = N\frac{f_c(\frac{n}{N}) + f_v(\frac{n}{N}) - 1}{f_c(n) + f_v(n) - 1} \tag{4.2}$$

For devices with high threshold gain requirements, the threshold current may be lower for a MQW than a SQW laser.

A double quantum well laser with the same confining structure as the SQW mentioned in the previous section was grown, except that as an active region we used two 5 nm quantum wells spaced by 8 nm. Figure 4.3 shows J_{th} vs. 1/L for the DQW broad area laser superimposed on the SQW laser data. The transparency current is about 50% higher; however, the slope $\frac{dJ_{th}}{d(\frac{1}{L})}$ is less, so for short cavity lasers the threshold current will be less. Because the gain requirement for high frequency passive mode-locking experiments are high, multiple quantum well material is preferred. From this DQW material we have made two section lasers producing passively mode-locked pulses at 120 GHz repetition rate [1].

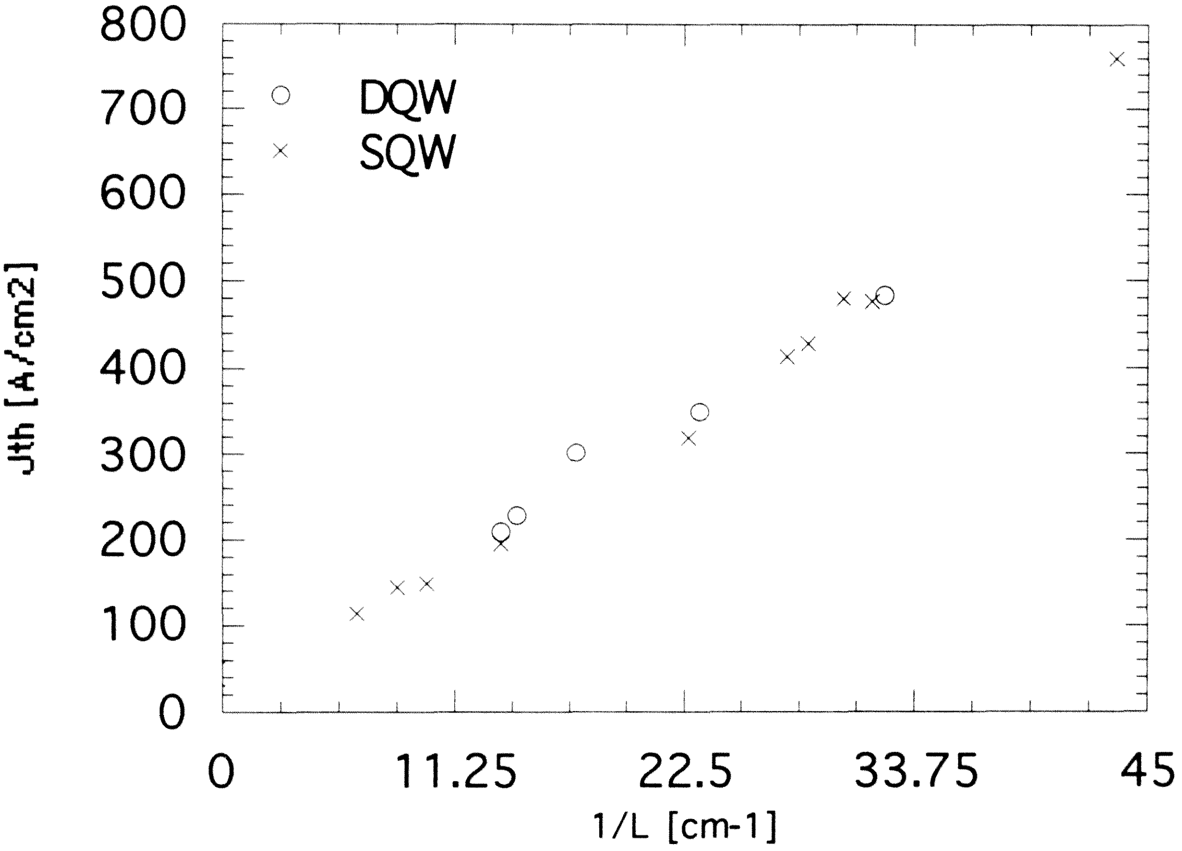

Figure 4.3: Threshold current density vs. 1/L for broad area InGaAs DQW lasers shown together with SQW data.

4.5 Low Threshold Buried Heterostructure Lasers

To achieve ultra-low threshold current devices, we need to minimize the active region volume while maintaining the integrity of the material. The structure must provide index guiding of the optical mode in the lateral direction, as well as confine the current to the quantum well. The buried heterostructure shown in Figure 4.4 is the best structure to date in accomplishing this goal. The fabrication involves surrounding the active region with higher bandgap, and hence lower refractive index, material epitaxially regrown by Liquid Phase Epitaxy (LPE). The fabrication is as follows: First, mesas with active regions of 2 μm are chemically etched down to the substrate. Then, the stripes are oriented along the (110) direction and the etched cross section has a "dove tail" shape. This cross section maximizes the contact area for a given active region width. Immediately prior to loading into a Liquid Phase Epitaxy (LPE) system for regrowth, the GaAs cap layer is removed to avoid growing on top of the ridge. The regrowth is done in two steps. First $p - Al_{0.5}Ga_{0.5}As$ to the junction plane is grown, and then $n - Al_{0.5}Ga_{0.5}As$ to the top is grown, both at 800 $°C$. This provides a reverse P-N junction in the AlGaAs when the diode is forward biased which blocks leakage current in these layers. Later, a contact region must be formed with a Zn diffusion in the top layer. After regrowth, the devices are cleaved and mounted, junction side up, on a copper heatsink. The lasing wavelength of the finished lasers was 950 nm, a shift of 40 nm from the unprocessed devices. We believe that the high temperature in the LPE furnace causes an interdiffusion of the InGaAs and the GaAs

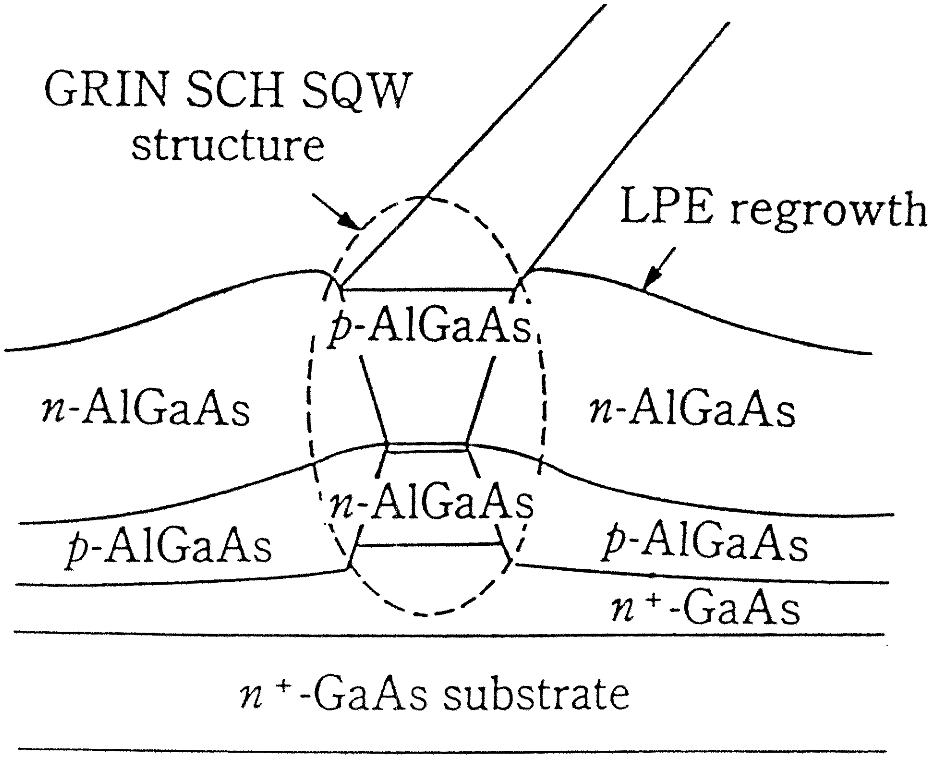

Figure 4.4: Schematic of buried heterostructure laser.

spacers. Similar observations have been reported elsewhere[12]. As with the broad area devices, we characterize the lasers with threshold current density vs. 1/L. The results are shown in Figure 4.5. Comparing this data with the broad area devices in figure 4.2, we see that threshold current densities in the regrown structure is still very low, and has increased by around 50% compared with the broad area lasers. This is a small price to pay for the 50X reduction in active region volume. A minimum $J_{th} = 167\frac{A}{cm^2}$ for a $1676\mu m$ long cavity is compared with $J_{th} = 114\frac{A}{cm^2}$ for a 1540 μm long broad area laser. Again we measure the differential quantum efficiencies to extract the internal loss constant and find $\alpha_i = 3.1cm^{-1}$. Using the linearized threshold current equations from chapter 2 and data from our devices, we find that our BH devices obey

$$J_{th} = 80\frac{A}{cm^2} + 5.8\frac{A}{cm^2}(\frac{1}{L})\log(\frac{1}{R_1R_2}) \tag{4.3}$$

and thus

$$I_{th} = 80WL\frac{A}{cm^2} + 5.8\frac{A}{cm^2}W\log(\frac{1}{R_1R_2}), \tag{4.4}$$

where W is the active region width. The linear gain regime for these lasers is seen to be for cavity lengths of

$$L > \frac{5.8log(\frac{1}{R_1R_2})}{400}[cm] \tag{4.5}$$

The lowest threshold current for these lasers is 1.65 mA for a 338 μm long device, which is still the lowest threshold current to date for these structures. The cavity length at which the threshold reaches a minimum is longer than for similar GaAs lasers ($L_{opt} = 200\mu m$) . This observation is consistent with a lower available maximum gain

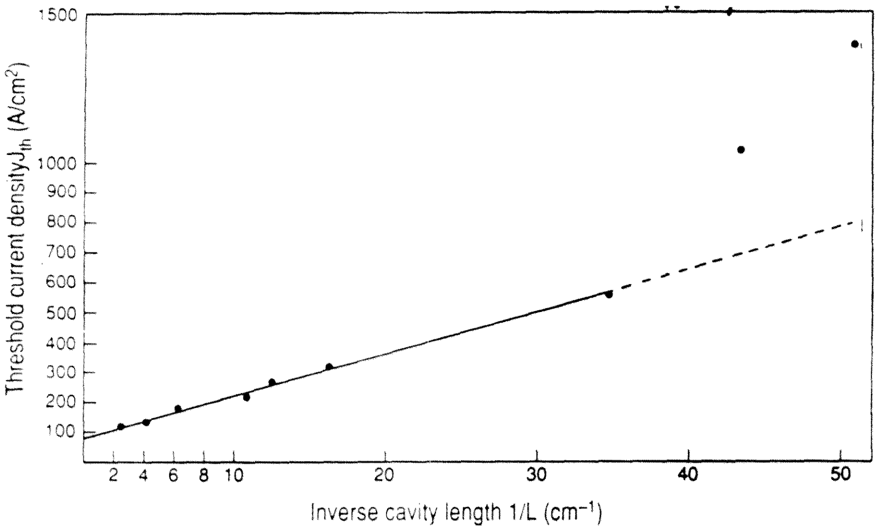

Figure 4.5: Measured threshold current density vs. 1/L for buried heterostruture InGaAs SQW lasers.

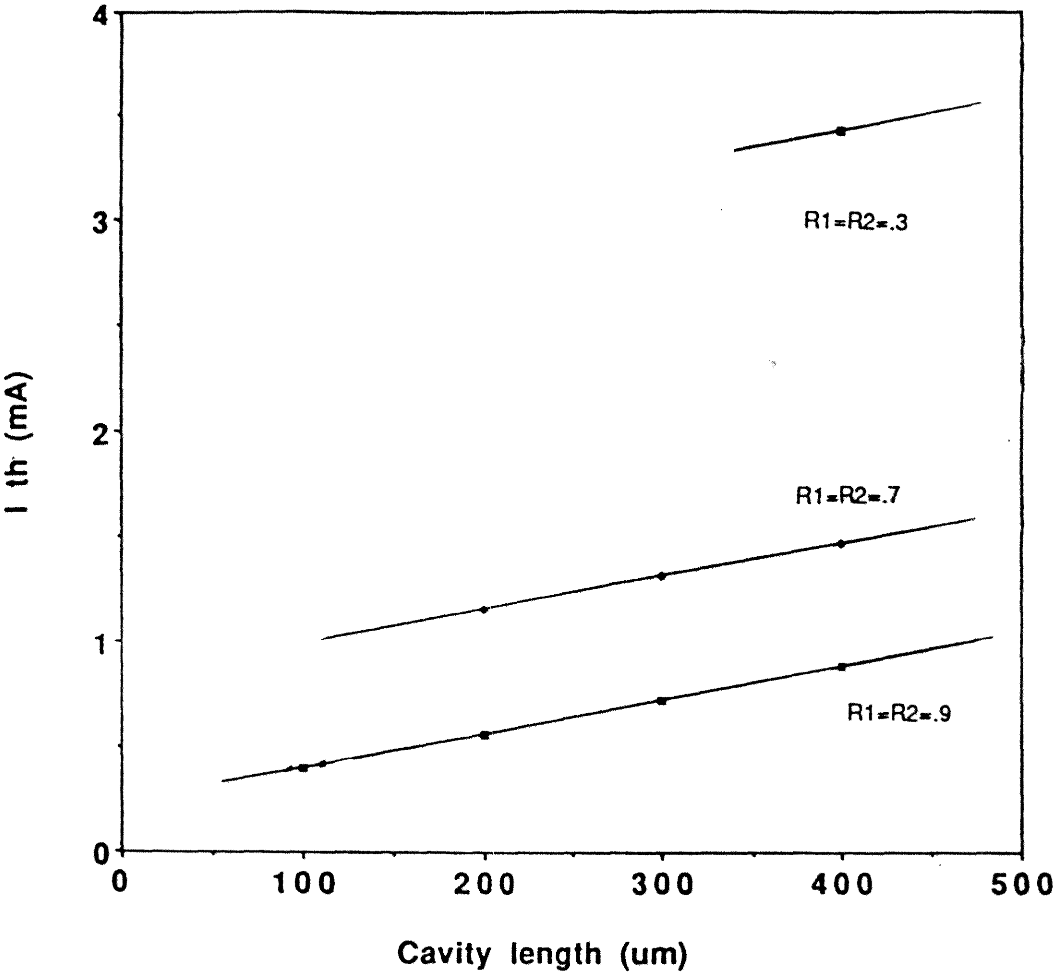

Figure 4.6: Predicted threshold current for BH lasers vs. cavity length.

in InGaAs material.

To further minimize the threshold current, we apply high reflectivity coatings to the mirrors in order to lower the mirror loss term. Plotting equation 4.4 as a function of cavity length and for various mirror reflectivities, we can obtain values of I_{th} we expect for our devices. This plot is shown in figure 4.6. We predict a

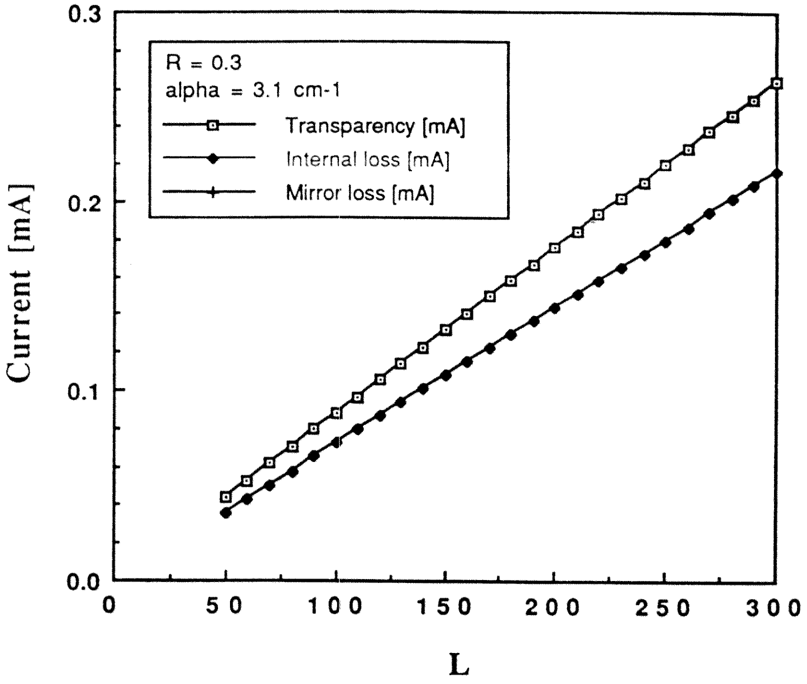

Figure 4.7: Estimated current components at threshold vs. cavity length for R = 0.3

minimum threshold current of $I_{thmin} = 0.4mA$ for a cavity length of $100\mu m$ and mirror reflectivities of $R_1 = R_2 = 0.9$. For the given values of internal loss, transparency current, and differential gain, it is interesting to examine the various components of I_{th} as a function of cavity length. Figure 4.7 shows the I_{th} components of an uncoated laser. It is clear that the mirror loss term is the dominant loss for all cavity lengths of interest. Therefore, it does not matter how much the transparency or internal loss is reduced, the threshold current will be virtually unchanged. Note, however, that the mirror loss component can be reduced by an increased differential gain in addition to increasing the mirror reflectivity. The I_{th} components of the same laser with 90% reflectivity coatings are shown in figure 4.7. The mirror loss is of the same order as

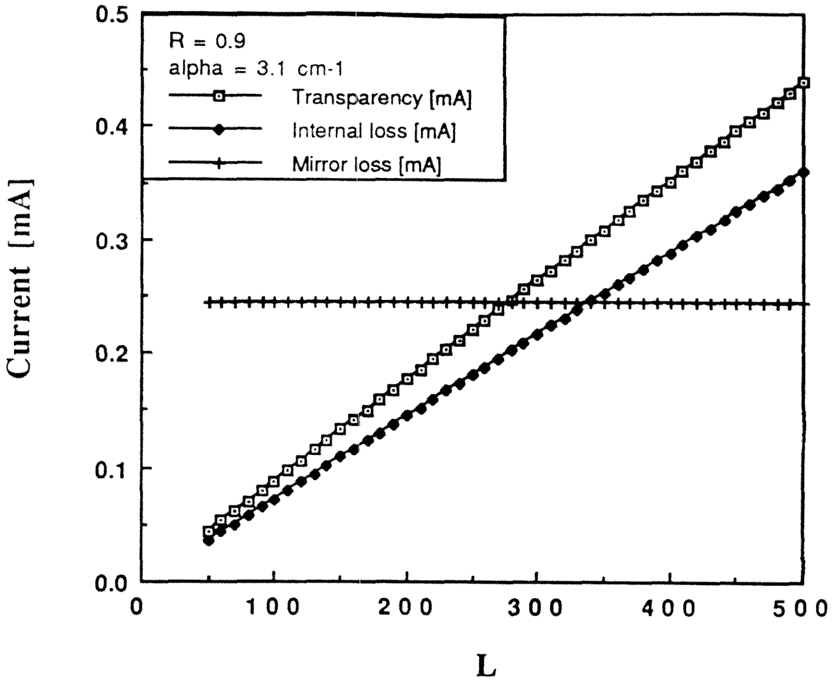

Figure 4.8: Current components at threshold vs. cavity length for R = 0.9.

the other loss components, and is actually less than the other losses for cavity lengths greater than 300 μm.

Figure 4.9 shows the measured L-I curves for a $200\mu m$ long device without mirror coatings, with one side coated, and with both sides coated to 0.9. For the high reflectivity structure of this cavity length we predict a threshold of 0.5 mA. Experimentally we have obtained a minimum threshold current of $I_{th}^{min} = 0.75mA$ This threshold is comparable to the best devices in GaAs[13,12] and is the lowest value reported for strained layer single quantum well material. Recently [15], we have improved this result to $I_{th}^{min} = 0.35mA$ which is record low for any single quantum well laser in any material system.

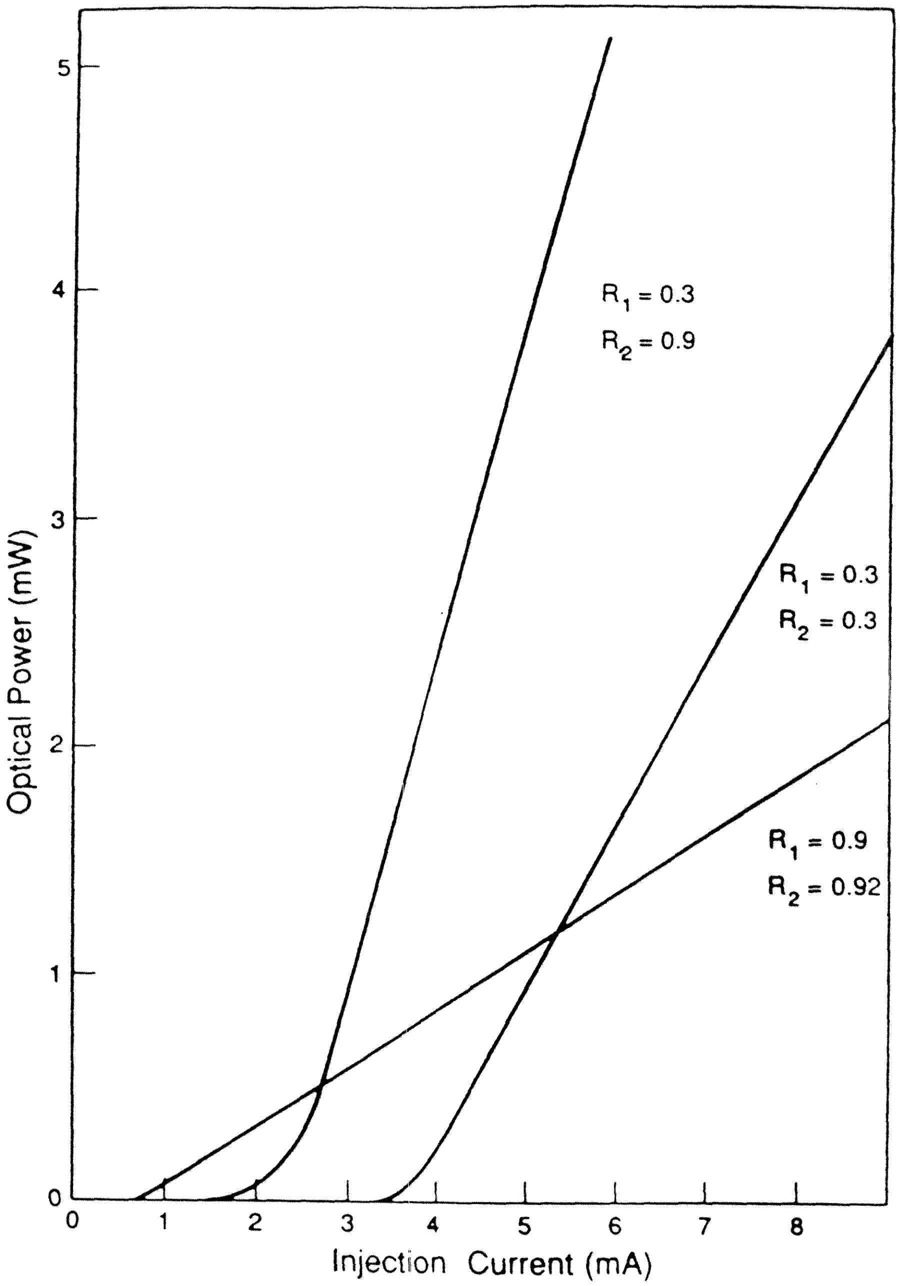

Figure 4.9: Light output vs current input for 200 μm long laser.

4.6 Improvements in Performance

As stated earlier in this chapter, the device structure grown was identical to our GaAs structure, and is by no means optimized for the InGaAs quantum well. Due to the lower bandgap of InGaAs, the AlGaAs barriers in the laser structure can have the aluminum mole fraction ramped from 0 (pure GaAs) to 70% in the cladding while still providing the same current barrier height as in the GaAs quantum well case. To see the improvement in the optical confinement we can calculate the optical confinement factor by approximating the parabolic waveguide by a three layer waveguide of indices n_1 and n_2 as in figure 4.10. It has been shown [17,6] that the shape of the index waveguide does not significantly alter the magnitude of the confinement factor, but affects the optimum width. Thus, the step index waveguide is a good approximation for determining possible enhancements in the confinement factor.

For a TE mode polarized along **y**, propagating in the z direction with a propagation constant β, we can write the lowest order transverse mode within the high index region as

$$E_y = E_0 cos(\kappa x) e^{i(\omega t - \beta z)}. \tag{4.6}$$

and in the low index region as

$$E_y = E_0 e^{-\gamma x} e^{i(\omega t - \beta z)}. \tag{4.7}$$

Using the boundary conditions at $|x| = d/2$, we find that the propagation constant β

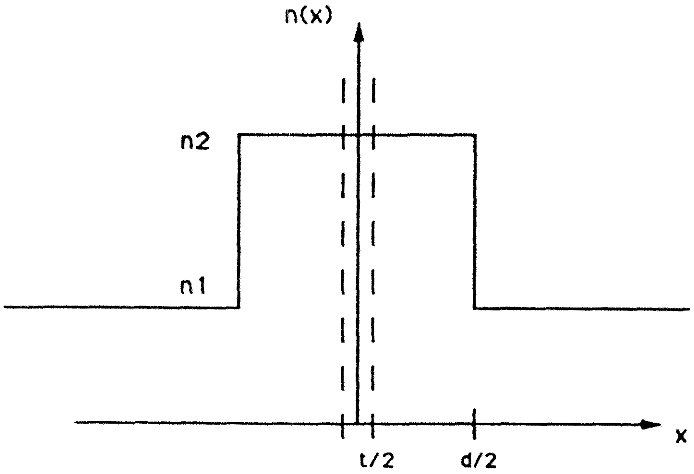

Figure 4.10: Three layer waveguide used to approximate the optical confinement in GRINSCH lasers.

is related to κ via the transcendental equation

$$(\frac{\kappa d}{2})tan(\frac{\kappa d}{2}) = \frac{\gamma d}{2} \tag{4.8}$$

with γ defined by

$$\kappa = ((n_2 k_0)^2 - \beta^2)^{\frac{1}{2}} \gamma = (\beta^2 - (n_1 k_0)^2)^{\frac{1}{2}}, \tag{4.9}$$

where $k_0 = \frac{2\pi}{\lambda_0}$ and λ_0 is the free space wavelength. For the three layer waveguide, the overlap of the optical power with the active quantum well region is then given by the analytic expression

$$\Gamma = \frac{t + \frac{1}{\kappa} sin(\kappa t)}{d + \frac{1}{\kappa} sin(\kappa d) + \frac{2}{\gamma} cos^2(\frac{\kappa d}{2})}, \tag{4.10}$$

where d is the waveguide width and t is the quantum well width. A plot of Γ vs. waveguide width d is shown in figure 4.11 for the two waveguides: the already grown structure, consisting of index steps corresponding to aluminum molefractions of 0.2/0.5, and the improved structure of 0.1/0.7. We see that by increasing the index step, we can, for an optimized waveguide width, increase the confinement factor by 40%. If we let the relative confinement factor Γ_r equal $\frac{\Gamma_{improved}}{\Gamma_{actual}}$, the effect of the improved confinement factor can be illustrated by rewriting the threshold equation 4.4 in terms of Γ_r

$$I_{th} = W[L(J_0 + \frac{\alpha_i c_1}{\Gamma_r}) + \frac{c_1}{2\Gamma_r} log(\frac{1}{R_1 R_2})]. \tag{4.11}$$

Notice that the transparency, J_0, is unaffected by Γ_r. A plot of I_{th} vs. Γ_r for uncoated and coated (R = 0.9) mirrors is shown in figure 4.12. The projected decrease in

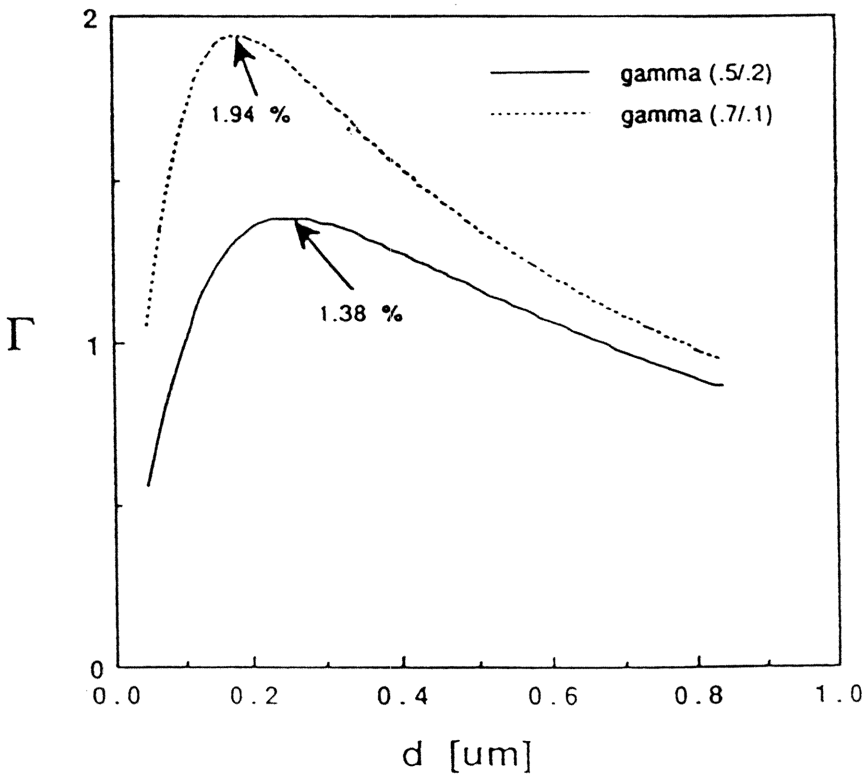

Figure 4.11: Confinement factor vs. waveguide width for the three layer waveguide.

threshold is much less for the coated lasers since the mirror loss term, where the main contribution to the threshold reduction comes, is already small. Thresholds will be reduced by 30% for an uncoated laser and 15% for the laser with high reflectivity coatings.

4.7 Conclusions

In conclusion, we have demonstrated the first sub milliampere threshold current in buried heterostructure InGaAs lasers. Threshold current densities in broad area ($w = 100\mu m$) lasers of $J_{th} = 114A/cm^2$ for cavity lengths of $L = 1540\mu m$. Transparency currents are approximately a factor of two lower than for GaAs lasers in agreement with calculations. Buried heterostructure devices lase at a threshold of $I_{th} = 1.0mA$ with as-cleaved facets, and $I_{th} = 0.35mA$ with high reflectivity mirror coatings (R = 0.9), which is record low for a single quantum well laser in any material system. Further improvements in the confinement structure are proposed to take full advantage of the InGaAs quantum wells.

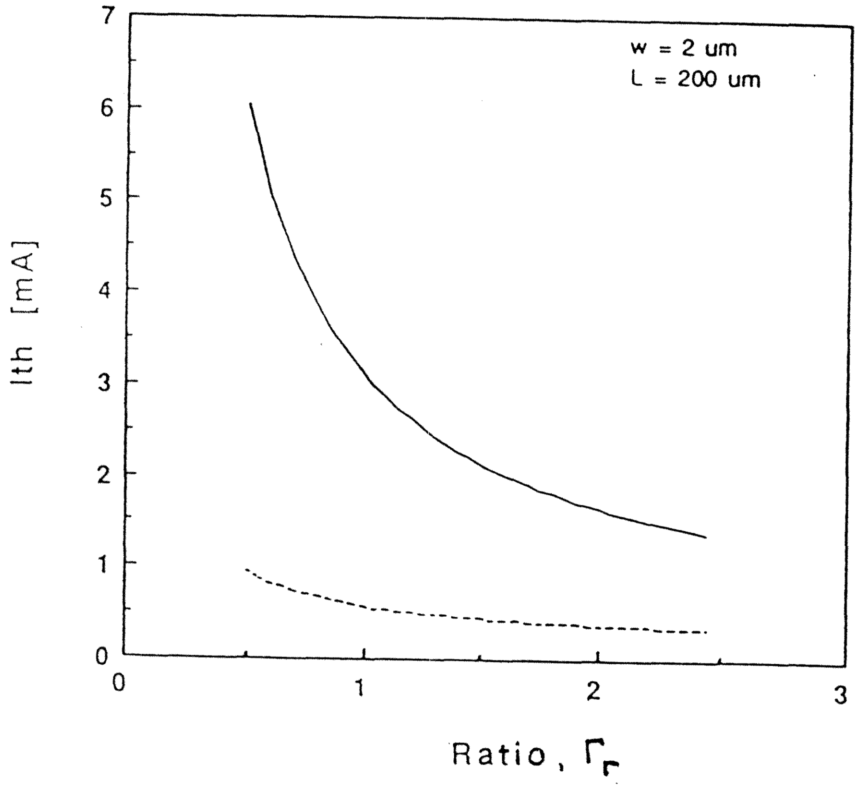

Figure 4.12: Projected improvement of threshold current with increased optical confinement.

References

[1] L.E. Eng, T.R. Chen, S. Sanders, Y.H. Zhuang, B. Zhao, A. Yariv, and H. Morkoç, *Appl. Phys. Lett.* **55**, 14, 1379 (1989)

[2] T.R. Chen, L.E. Eng, Y.H. Zhuang, and A. Yariv, *Appl. Phys. Lett.* **56**, 11, 1002 (1990)

[3] R.G. Waters, P.K. York, K.J. Beernik, and J.J. Coleman, *J. Appl. Phys.* **67**, 1132 (1990)

[4] H.Z. Chen, A. Ghaffari, H. Morkoç, and A. Yariv, *Electron. Lett.* **23**, 1334 (1987)

[5] H.K. Choi, and C.A. Wang, *Appl. Phys. Lett.* **57**, 321 (1990)

[6] R.L. Williams, M. Dion, F. Chatenoud, and K. Dzurko, *Appl. Phys. Lett.* **58**, 1816 (1991)

[7] H.Z. Chen, A. Ghaffari, H. Morkoç, and A. Yariv, *Appl. Phys. Lett* **51**, 2094 (1988)

[8] L.P. Erickson, G.L. Carpenter, D.D. Seibel, P.W. Pearah, W. Kopp, and H. Morkoç, *J. Vac. Sci. Technol.* **B3**, 536 (1985)

[9] H. Hirayama, Y. Miyake, and M. Asada, *IEEE J. Quant. Electr.* **28**, 68 (1992)

[10] J. Nagle, M. Hersee, T. Weil, and C. Weisbuch, *Appl. Phys. Lett.* **49**, 719 (1985)

[11] S. Sanders, L.E. Eng, and A. Yariv, *Electron. Lett.* **26**, 1087 (1990)

[12] R. M. Kolbas, Y.J. Yang, and K.Y. Hsieh, *Superlattices and Microstructures* **4**, 603 (1988)

[13] P. Derry, A. Yariv, K. Lau, N. Bar-Chaim, K. Lee, and J. Rosenberg, *Appl. Phys. Lett.* **50** 1773 (1987)

[14] K. Lau, P. Derry, and A. Yariv, *Appl. Phys. Lett.* **52**, 88 (1988)

[15] To be published

[16] A. Yariv, *Quantum Electronics*, 3^{rd} edition, Wiley (1989)

[17] W. Streiffer, R.D. Burnham, and D.R. Scifres, *Opt. Lett.* **8**, 283 (1983)

[18] S. Chinn, *Appl. Opt.* **23**, 3508 (1984)

Chapter 5

Broadband Tuning of InGaAs Quantum Well Lasers

5.1 Introduction

Tunable compact semiconductor laser sources are an attractive alternative to solid state and dye laser systems pumped with high power gas lasers. Semiconductors can exhibit broadband gain and can emit radiation over a wide spectrum under proper operating conditions. Quantum well lasers, in particular single quantum well lasers, can take better advantage of this bandwidth than bulk double heterostructure lasers due to their small active region volume and, therefore, larger band filling at the same current density. This large bandwidth can be useful in creating short mode locked pulses [1], and for applications where broadband tunability is desired [2]. The use of InGaAs for the active region of the laser permits the lasing to be extended beyond

$1 \mu m$ which includes the 980 nm wavelength of current interest for pumping Er^+ doped fiber amplifiers. In this chapter, we report on the broadband tuning properties of strained InGaAs quantum well lasers and compare them with GaAs quantum well lasers optimized for this purpose. Our InGaAs lasers have been tuned over 170 nm, a much wider range than in previous reports [3], and we observe a difference in the tuning characteristics compared with GaAs lasers.

5.2 Quantum Wells for Tuning

An optimal laser for tunability has a perfectly flat gain spectrum so that a wavelength dependent loss mechanism can select the desired lasing wavelength without a large increase in bias current. As discussed in chapter 2, single quantum well lasers, with parabolic conduction and valence bands, have a step-like reduced density of states vs. energy profile. The width of the first flat step is given by the separation of the e1-h1 (n=1) and e2-h2 (n=2) transition energies in the quantum well, and it is the width of this step which we would like to maximize for broadband tuning. Although it isn't necessary to limit the lasing to the first subband, the resulting threshold currents will be much lower due to the lower number of states to fill to reach inversion. A narrow, deep quantum well is desirable to separate the two subbands as far as possible. The limit is reached when the second state is pushed out of the well and into the confining region, which drastically increases the threshold current. So, the tuning is limited on the short energy side by the bandgap of the well material, and on the high energy side by the bandgap of the confining material. Once optimized, the laser is then operated under conditions where most of the states between these levels are populated with carriers, and lasing can then occur at any of these energies given the proper feedback. The operating condition for maximum tuning range in GaAs quantum wells has been found to be a threshold gain such that the laser just operates in the second quantized state [4,5] before adding any feedback. Calculated [4] gain vs. energy curves [4] for a single GaAs quantum well laser with parabolic energy bands is shown in Figure 5.1. The laser cavity is cleaved short enough to lase in the n=2 transition and without feedback lases at λ_0. With feedback the lasing occurs at λ_1 with a threshold current of J_1. The resulting threshold current vs. tuned wavelength is illustrated below in the same figure.

5.3 Oxide Stripe Lasers and Tuning Results

The optimized GaAs lasers have a $60\mathring{A}$ quantum well with $Al_xGa_{1-x}As$ graded barriers, where x is graded parabolically from 0.4 to 0.7. The cavity length is cleaved just short enough to lase free running (without feedback) in the $n = 2$ state . A diffraction grating is used to provide feedback in an external cavity configuration as shown in Figure 5.2. The grating feeds back one wavelength, and therefore raises the effective facet reflectivity there. The lowered loss fixes this lasing wavength and this selective feedback provides the mechanism for tuning. The wavelength range over which we can tune the GaAs laser is from 730 to 855 nm, a record 125 nm.

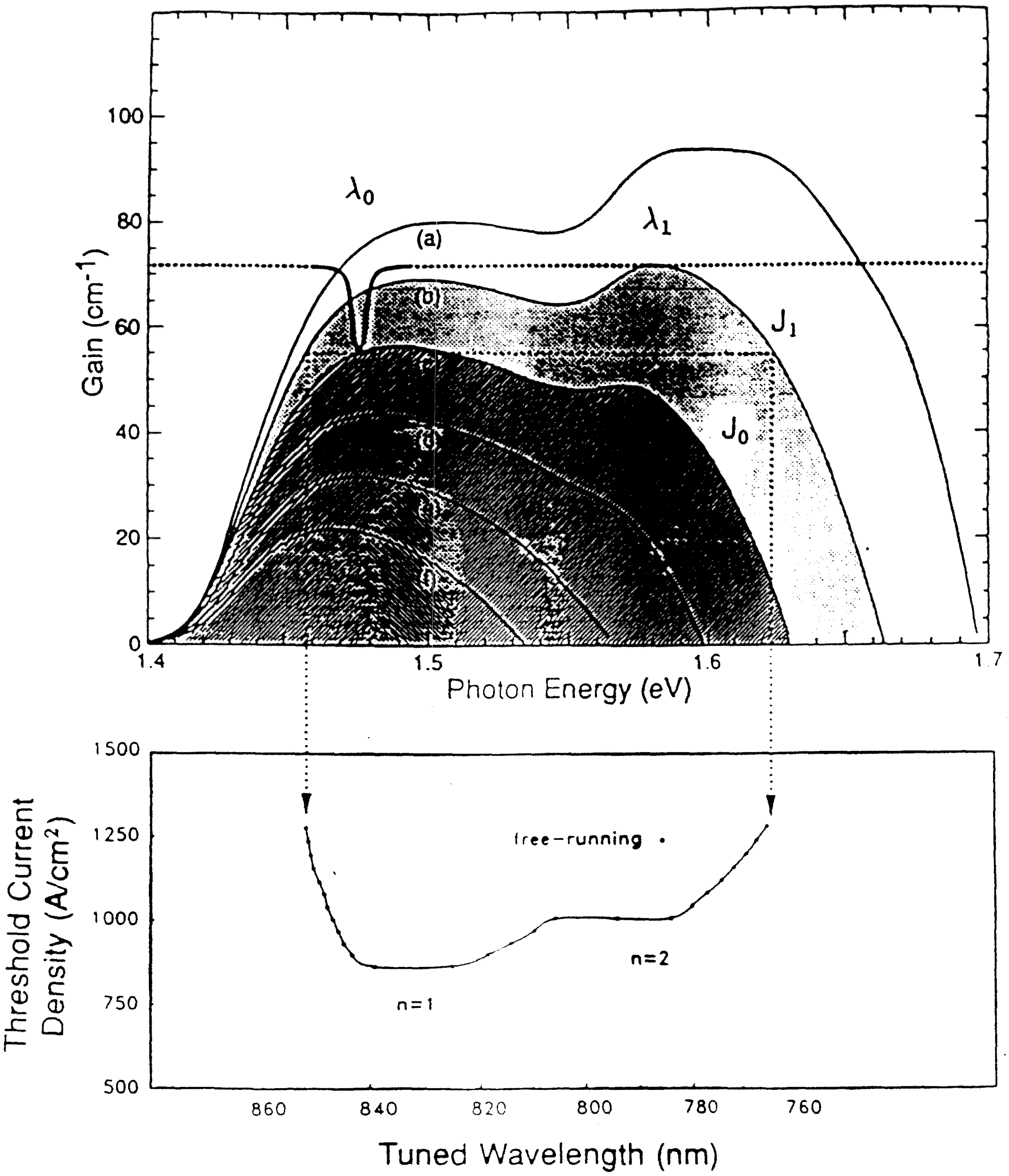

Figure 5.1: Above: Calculated gain vs. photon energy for a GaAs quantum well laser assuming parabolic bands for various pumping levels (from Reference [2]). Below: The resulting threshold current vs. grating tuned wavelength.

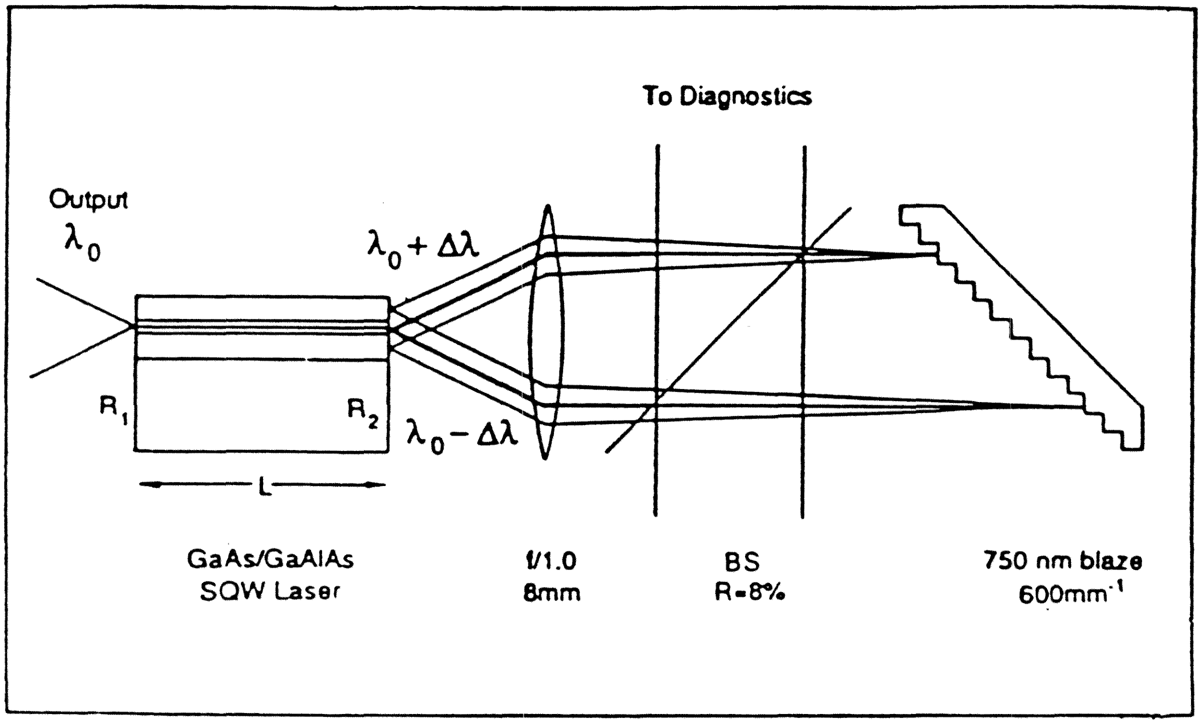

Figure 5.2: Configuration for wavelength tuning in an external cavity.

To extend the tuning range to shorter wavelengths, it is necessary to confine the carriers with a higher barrier than is available in $Al_xGa_{1-x}As$. To access longer wavelengths, however, an active region of lower band gap material must be used. With a lower bandgap material, the relative barrier heights are now larger, permitting the use of a narrower well. This increases the energy subband separation and hence, the absolute tuning range. $In_yGa_{1-y}As$ has a lower band gap than GaAs and, when used as the active region in quantum well lasers, has been shown to emit at wavelengths as long as $1.1\mu m$ [6]. Although the $In_yGa_{1-y}As$ is not lattice-matched to the GaAs substrate, high quality devices, i.e., devices with low threshold currents [11] and high quantum efficiencies [8], can still be fabricated since the thin wells in these structures are less than the critical layer thickness [9] for this material system. Figure 5.3 is a calculation of the two lowest transitions in a $50\mathring{A}$ strained quantum well with $Al_{0.4}Ga_{0.6}As$ barriers as a function of indium content. The difference in these energies is a good indication of the possible tuning range of strained InGaAs quantum well lasers. We have examined the tunability of an $In_yGa_{1-y}As$ quantum well structure bounded by a GaAs spacer and an $Al_xGa_{1-x}As$ (x=0.2 - 0.5) graded region for confinement of the optical mode.

The $50\mathring{A}$ $In_{.35}Ga_{.65}As$ single quantum well strucure was grown on a GaAs substrate by molecular beam epitaxy (MBE) and has a $40\mathring{A}$ GaAs spacer layer on each side. Details of the growth conditions have been given in a previous chapter. From this low threshold current material, $10\mu m$ wide stripe ridge waveguide lasers were fabricated and tested. We cleaved lasers of various lengths and measured the emission

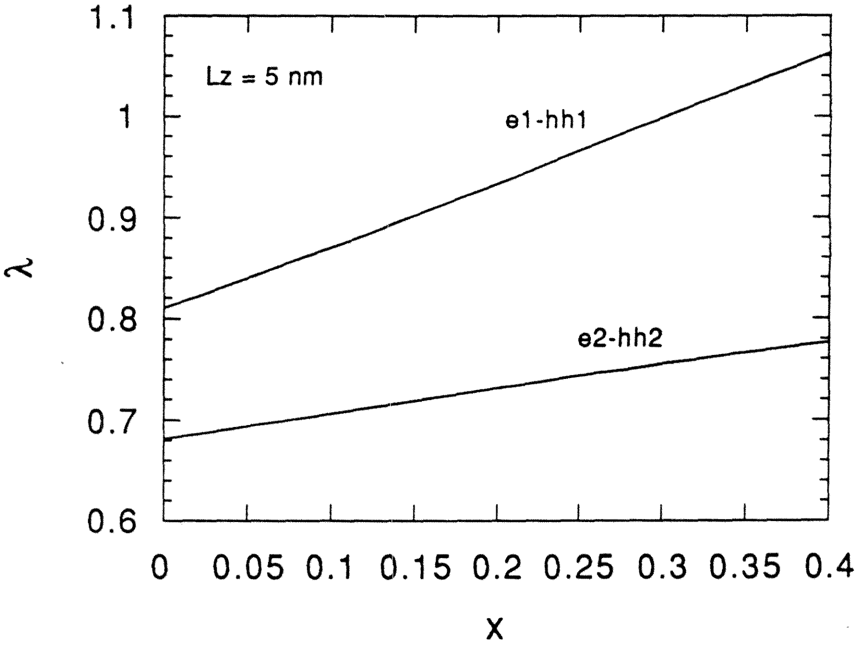

Figure 5.3: Calculated el-h2 and e2-h2 band edge transition wavelengths for a strained InGaAs quantum well with $Al_{0.4}Ga0.6As$ barriers

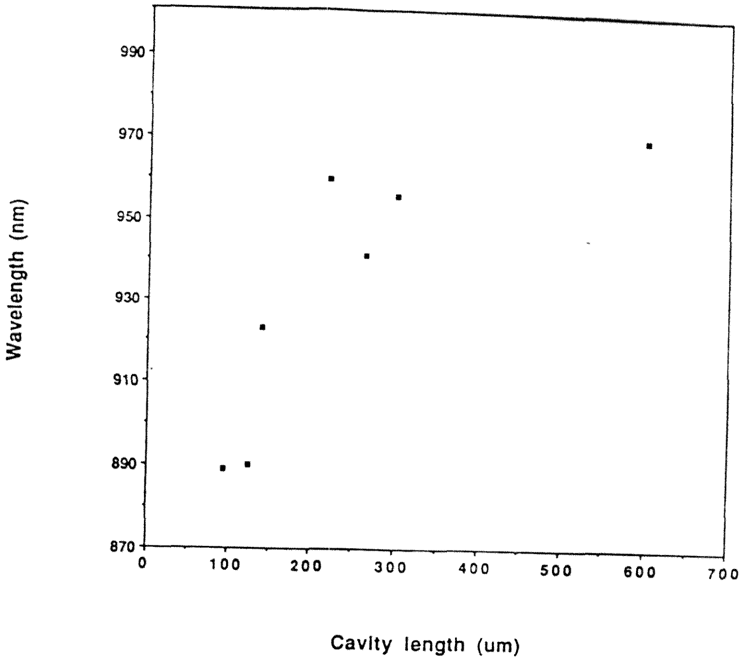

Figure 5.4: Measured lasing wavelength vs. cleaved cavity length for InGaAs $10\mu m$ wide ridge waveguide lasers used for tuning.

wavelength versus cavity length, L, which is shown in Figure 5.4. A sharp transition to shorter wavelengths is apparent for $l < 150\mu m$, which we attribute to the $n = 2$ lasing state [4]. For the tuning experiments, the lasers were uncoated, and operated pulsed at low duty cycle and placed in the external cavity with the grating. Results from the tuning measurements are presented in figure 5.5, where we have plotted threshold current as a function of tuned wavelength.

As a comparison, we also show the tuning characteristic of an optimized GaAs quantum well laser. The InGaAs laser oscillates over $170nm$, which is to be compared with $125nm$ for the best GaAs laser. To our knowledge these are the widest published

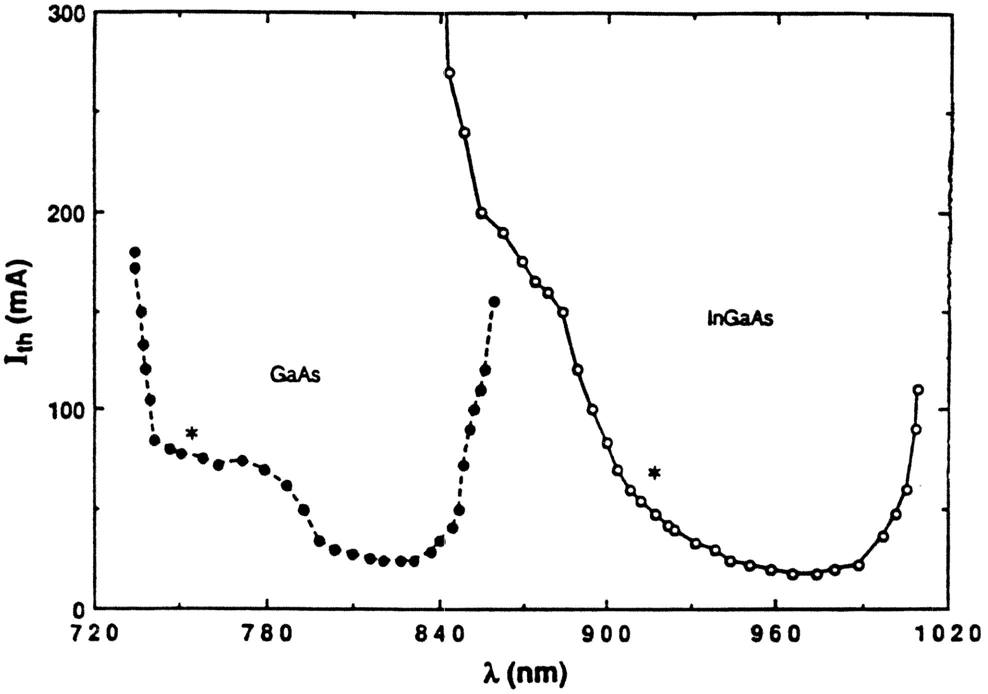

Figure 5.5: InGaAs and GaAs broadband tuning results.

tuning ranges for these material systems. The threshold currents are comparable for the two lasers and are low enough to permit CW operation. Also, in agreement with other work [3] we see that we are able to tune into GaAs wavelengths without problems.

5.4 Comparison of InGaAs and GaAs Tuning

Our measurements indicate, however, that the tuning characteristics of InGaAs lasers are qualitatively different from the GaAs lasers. For GaAs lasers we have seen, from calculations of gain spectra and previous tuning measurements, that the spectral gain saturates at high current injection, and is relatively flat just at the onset of second quantized state lasing, in agreement with the simple theory [4]. When the gain requirement of the resonator is set too high, an abrupt reduction in tuning range is experienced since the n=1 transitions are no longer accessible [5]. However, for InGaAs lasers, we observe a gradual loss of tuning on the long wavelength side upon increasing the gain requirement. We have measured the tunability of InGaAs lasers of various cavity lengths, shown in figure 5.6, and found that as we shorten the cavity length the tuning range on the long wavelength side decreased. This indicates that the maximum available gain from the $n = 1$ transitions in the strained lasers is not as flat as for unstrained GaAs quantum well lasers. The results suggest that the maximum gain from $n = 1$ transitions is significantly lower at the longer wavelengths, and the feedback from the grating is not sufficient to overcome the losses.

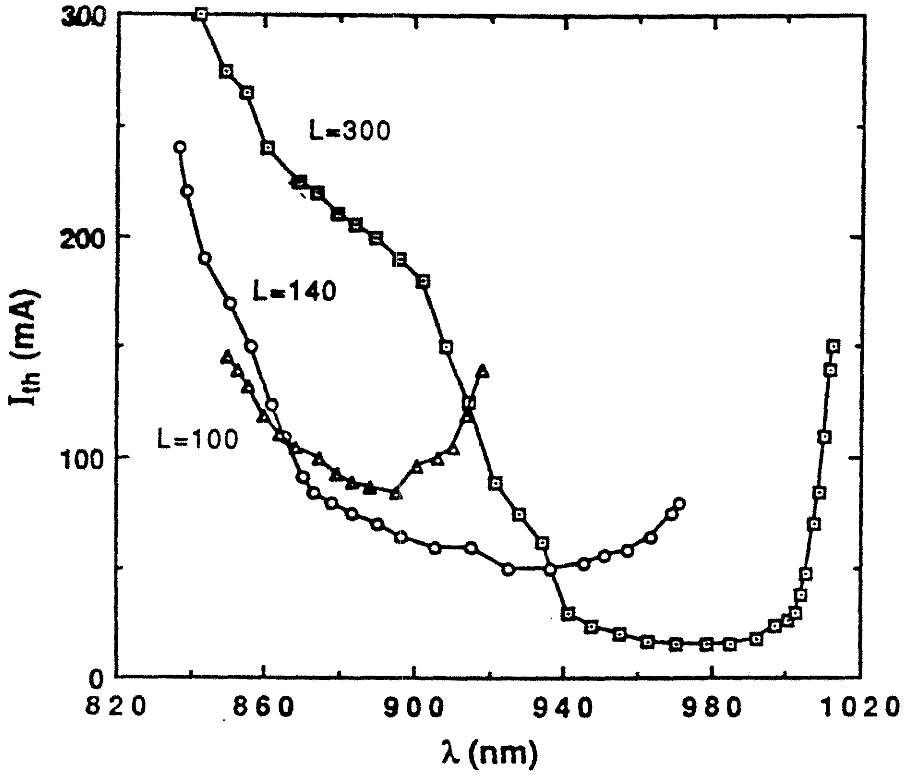

Figure 5.6: InGaAs tuning for various cavity lengths.

Our experimental results, in particular the difference in tuning characteristics of InGaAs and GaAs, can be explained by considering a simple model for the maximum achievable gain. When operating at high current densities, the gain at a given wavelength reaches a maximum value and, to a first approximation, follows the spectral distribution of the density of interband transitions. From energy band calculations by Suemune et al. [14], the valence band density of states (D.O.S.) is an increasing function of hole energy in strained InGaAs quantum wells, and can increase by as much as a factor of 3 in the first quantized state. The reduced D.O.S. is given by

$$\rho_r = \frac{\rho_v}{1 + \frac{\rho_v}{\rho_c}} \tag{5.1}$$

and thus we see that the maximum gain is increased by a factor of 1.5 when $\frac{\rho_v}{\rho_c}$ increases from a value near unity at the first sub band edge compared with its value near 3 just below the second sub band edge. If we scale the gain constant of GaAs with effective mass, we see that the absolute gain difference is on the order of $35cm^{-1}$, which can explain our observations. A more detailed calculation of the modal gain constant vs. wavelength is shown in Figure 4. Here we have used the data published by Suemune et al. [14] for the valence band D.O.S., assumed a constant electron effective mass, and a matrix element equal to that of GaAs. These calculations suggest that the modal gain at 1000 nm is limited to 50 cm^{-1} no matter how strong the pumping, while the maximum available gain at 900 nm is more than 1.5 times larger. Consequently, the gradual loss in tuning at long wavelengths can be due to the nonparabolicity in the valence band.

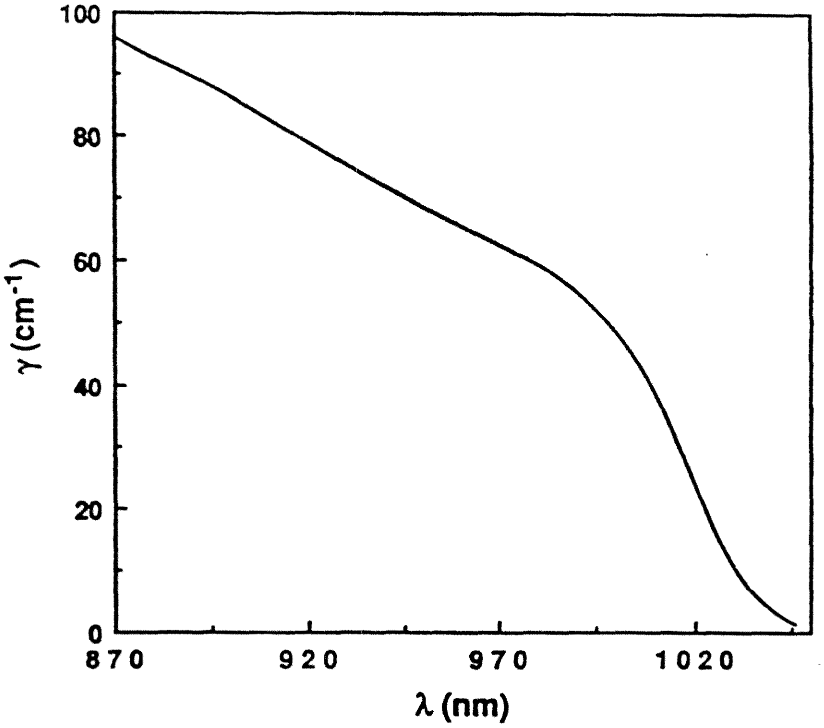

Figure 5.7: Calculated maximum gain using the strained valence band density of states given in Reference [14]

5.5 Conclusions

In conclusion we have used a grating in an external cavity to tuned InGaAs quantum well lasers over 170 nm, more than 40 nm greater than previous reports. Together with an optimized GaAs laser operated in the same configuration, we see that the entire region between 740 nm and 1010 nm can be spanned. In the course of these measurements, we have detected a different behavior between the strained and unstrained lasers, corresponding to a different shape of spectral gain curves for the two types of lasers. A possible explanation is an energy dependent valence band effective mass in the strained laser.

References

[1] S. Sanders, L.E. Eng, J. Paslaski, and A. Yariv, *Appl. Phys. Lett.* **56**, 310 (1990)

[2] M. Mittelstein, D. Mehuys, A. Yariv, J. Ungar, and R. Sarfaty, *Appl. Phys. Lett.* **54**, 1092 (1989)

[3] D.C. Hall, J.S. Major, N. Holonyak, P. Gavrilovic, K. Meehan, W. Stutius, and J.E. Williams, *Appl. Phys. Lett.* **55**, 752 (1989)

[4] M. Mittelstein, Y. Arakawa, A. Larsson, and A. Yariv, *Appl. Phys. Lett.* **49**, 1689 (1986)

[5] D. Mehuys, M. Mittelstein, A. Yariv, R. Sarfaty, and J.E Ungar, *Electron. Lett.* **25**, 143 (1989)

[6] R.G. Waters, P.K. York, K. Beernik, and J.J. Coleman *J. Appl. Phys.* **67**, 1132 (1990)

[7] L.E. Eng , T.R. Chen, S. Sanders, Y.H. Zhuang, B. Zhao, H. Morkoç, and A. Yariv, *Appl. Phys. Lett.* **55**, 1378 (1989)

[8] A. Larsson, J. Cody, and R. Lang, *Appl. Phys. Lett.* **55**, 2268 (1989)

[9] I.J. Fritz, S.T. Picraux, L.R. Dawson, T.J. Drummond, W.D. Laidig, and N.G. Andersson, *Appl. Phys. Lett.* **46**, 967 (1985)

[10] I. Suemune, L.A. Coldren, M. Yamanishi, and Y. Kan, *Appl. Phys. Lett* **53**, 1378 (1988)

Chapter 6

Microampere Threshold Current Operation of GaAs and Strained InGaAs Quantum Well Lasers at Low Temperatures

6.1 Introduction

Although the effect of temperature on the operation of semiconductor lasers has been studied extensively, most papers are concerned with temperatures near and above 300° K [1]-[8]. In these cases, a laser with a low sensitivity to temperature variation is desirable for stability purposes. In some systems, for example antennas used in space applications [9], electronic devices and circuitry may be at cryogenic temperatures.

For the potential use of optical interconnects in this circuitry, it is desirable to know the laser properties at these temperatures. Here, a large sensitivity to temperature is an advantage since the lowest achievable I_{th} will be lower.

Low temperature operation, in particular down to temperatures as low as 5° K, has to our knowledge previously not been addressed. It has been shown that for bulk active regions, the threshold current increases exponentially with increasing temperature, whereas for quantum well lasers this relation only holds in limited regions. In either case, we expect a significant reduction in the threshold current when reducing the temperature to 5° K. In this chapter, we concentrate on the temperature dependence of threshold current and lasing wavelength in regions at and well below room temperature. We use a simple model to explain the observed differences in threshold behavior between GaAs and InGaAs lasers. Specifically, expressions for the transparency and threshold carrier densities as a function of temperature are derived for a single quantum well laser with carriers limited to one quantized state. At low temperatures, the higher subbands become less populated and these simple expressions will become more valid.

Early reports on the lasing threshold current density, J_{th}, as a function of temperature, found an exponential increase with T characterized by J_0 and T_0 [1],

$$J_{th} = J_0 e^{\frac{T}{T_0}} \tag{6.1}$$

However, more recently it has been found, both experimentally [8] and theoretically [3], that this relation only holds in a limited range of temperature, and that the parameters J_0, T_0 are strong functions of temperature and threshold gain. An expression which has been found to better characterize the temperature behavior is

$$J_{th}(T) = KT^x, \tag{6.2}$$

where x has been calculated for the non-degenerate case [3] to be 3/2, 1, 1/2 for bulk, quantum well, and quantum wire active regions.

6.2 Low Temperature Measurements

The lasers used in this experiment are buried heterostructures (BH) made from single quantum well graded index separate confinement heterostructure (GRINSCH) layers grown by Molecular Beam Epitaxy (MBE). For specifics on the laser structure and growth, we refer to Reference [11]. High reflectivity mirror coatings, $R1 = R2 = 0.9$, were applied to lower the end losses and to maximally reduce the threshold as discussed in chapter 3. The lasers were mounted junction side up using In solder, with Au wire bonds making the electrical connections. The devices were then attached to a larger copper block, acting as a heat sink, with a thermocouple attached for temperature measurement. Lasing threshold was defined as the extrapolated current value of the sharp turn-on of the light output vs. current curves (L-I) under continuous wave (CW) operation. These threshold current values, for both GaAs and InGaAs lasers, were then recorded as a function of mounting block temperature and are shown in figure 6.1.

The lasing wavelength was also measured, and the corresponding lasing energy

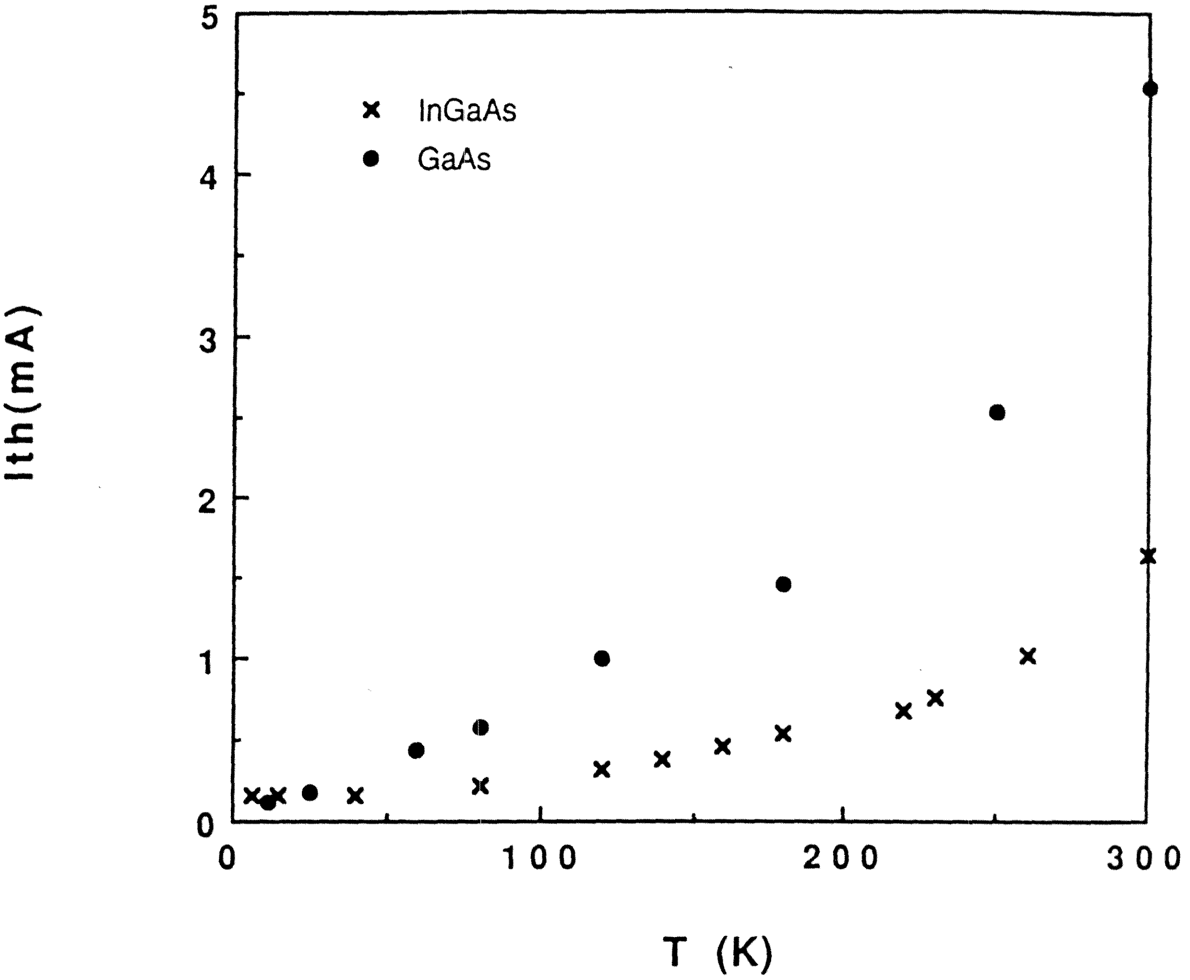

Figure 6.1: Threshold current vs. temperature for GaAs and InGaAs lasers.

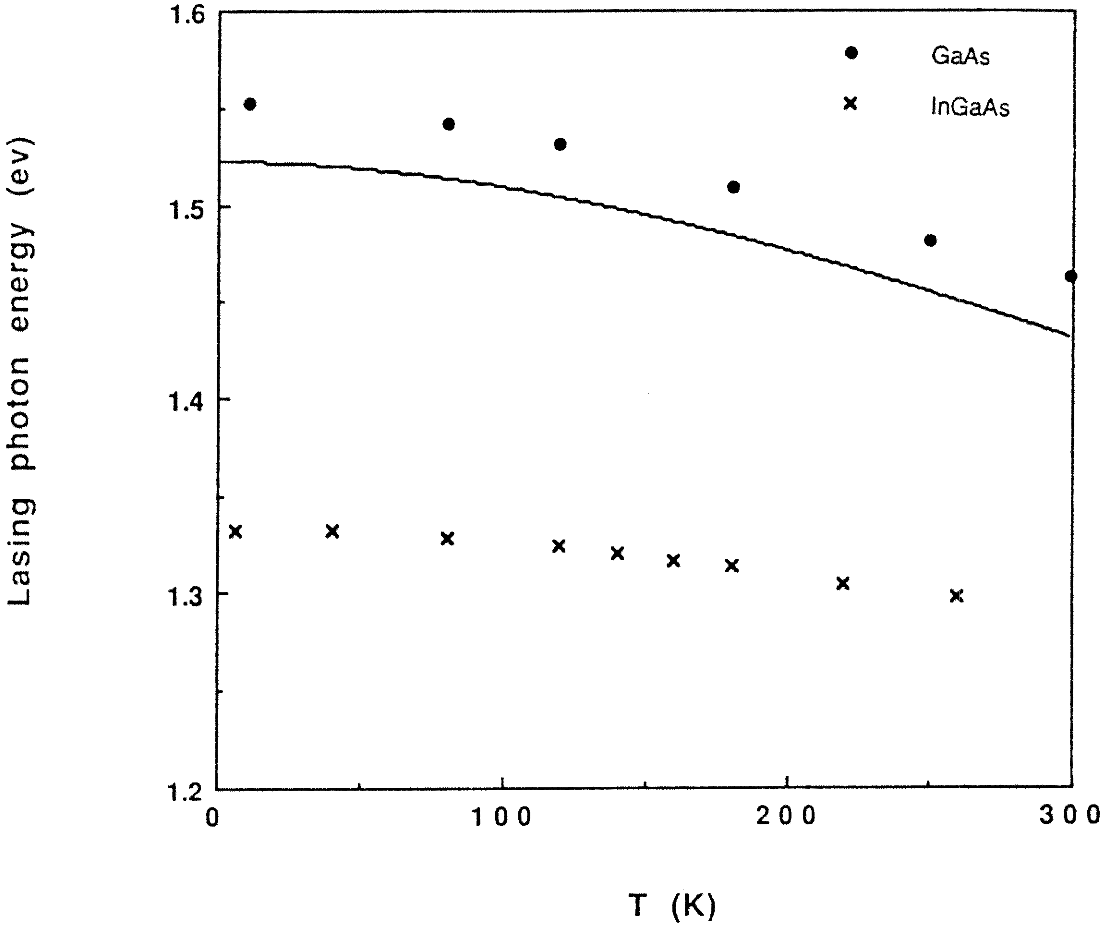

Figure 6.2: Lasing energy vs. temperature for GaAs and InGaAs BH SQW lasers.

	Ith [mA]		dIth/dT [μA/K]	dElaser/dT [meV/K]	
	5K	300K		5K	300K
GaAs	0.120	4.5	8.32	-0.14	-0.38
InGaAs	0.165	1.6	3.29	-0.18	-0.10

Table 6.1: Summary of low temperature measurements

as a function of temperature is displayed in Figure 6.2, along with the band gap variation of GaAs with temperature. The lasing energy of both lasers increases with decreasing temperature at a rate similar to the GaAs band gap. Some of the main properties of interest are assembled in table 6.1.

From Figure 6.1 we see that the laser with the GaAs active region starts out with a higher threshold current ($I_{th} = 4.5mA$) at room temperature than the InGaAs ($I_{th} = 1.6mA$), but decreases at a faster rate with temperature. Below $200^\circ K$, both laser thresholds fall nearly linearly with decreasing temperature. Also, we note a cross-over point at about 20° K below which the GaAs threshold is lower than the InGaAs. The ultimate achievable threshold current is lower for the GaAs laser, which reaches a minimum value of $120\mu A$. The InGaAs threshold levels off to a value of $165\mu A$ at 15° K and becomes constant. This effect is not seen in the GaAs lasers, and may be due to a residual leakage current .

6.3 Threshold vs. Temperature

We employ a simple model to explain the different slopes of the curves for the two types of lasers. At elevated temperatures and for high gain laser structures, the higher quantized energy levels in the active region and even in the barrier regions play a significant role in determining $I_{th}(T)$ [5,6]. Also, the quality of the barrier region has been shown to have a pronounced effect on $I_{th}(T)$ due to nonradiative recombination [7]. The effect of broadening, both in the transitions[6,7] and in the density of states [8], has been treated and has shown to influence T_0 in Equation (1) above significantly, but leaves the slope ,K, in Equation (2) unchanged. Since our analysis results in Equation 2, broadening should not have an effect on our model. Also, at low temperatures and for low loss lasers, it is reasonable to neglect the higher energy levels and include the $n = 1$ transitions only. Next, we model the addition of In to the active region of a GaAs laser by using a lowered valence band effective mass [12]. Finally, we derive an expression for the threshold carrier density, with the valence/conduction band effective mass ratio as a parameter.

6.4 Threshold Carrier Density

The threshold gain is given by

$$g_{th} = \alpha + \frac{1}{L} log \frac{1}{R} \tag{6.3}$$

and clamps the carrier density at threshold to n_{th}. Next, we assume that the losses are independent of temperature. This will especially be true at low temperatures since the internal losses due to free carriers and intervalence band absorption scale with n_{th} and n_{th}^3 respectively, will become much less than the constant mirror loss term. From chapter 2, the gain written in terms of the fermi factors and valence to conduction band mass ratio R is given by

$$g_m = \gamma_0 \frac{R}{R+1} (f_c + f_v - 1). \tag{6.4}$$

The fermi functions at the band edge, $E_c = 0$ and $E_v = 0$, including only one quantum well sub band, become

$$f_{c,v} = 1 - e^{-\frac{n_{th}}{n_{c,v}}} \tag{6.5}$$

for a carrier injection level n (= p). The term $n_{c,v}$ is the familiar two dimensional density of states multiplied by kT

$$n_{c,v} = \rho_{c,v} k_b T = \frac{m_{c,v} k_b T}{\pi L_z \hbar^2}. \tag{6.6}$$

Substituting into the threshold condition in equation 6.4, we arrive at an equation for the carrier density as a function of threshold gain:

$$(1 - \frac{g_{th}}{g_{max}}) - e^{-\frac{n_{th}}{n_c}} - e^{-\frac{n_{th}}{R n_c}} = 0, \tag{6.7}$$

where

$$g_{max} = \gamma_0 \frac{R}{R+1} \tag{6.8}$$

. Since g_{max} depends on R, this equation will be solved numerically. First we see, however, that if the threshold gain is independent of temperature, each of the other terms in the equation above must also be constant with respect to T. This means that the threshold carrier density has the same temperature dependence as n_c, i.e., it is linear. We can solve for the ratio β defined by

$$\beta = \frac{n_{th}}{n_c}$$

as a function of R.

β is a measure of the temperature sensitivity of the threshold carrier density and depends on the ratio of valence to conduction band density of states, R, through Equation (7). β increases with R and threshold gain. Intuitively, we can see this by examining the number of populated states above the fermi level which do not contribute to gain. The larger the density of states above E_{fc}, the larger the number of "wasted" carriers will be, as far as gain is concerned. Hence, a decrease in temperature causes a larger reduction in the number of carriers at threshold in a material with a larger density of states. Therefore, we expect the GaAs lasing thresholds to decrease faster with temperature than the InGaAs lasers.

We have plotted β in figure 6.3 only for cases such that the threshold gain is less than 70% of the maximum gain. β increases sharply beyond this point due to the saturation of the gain with current. In addition, the model will break down since this

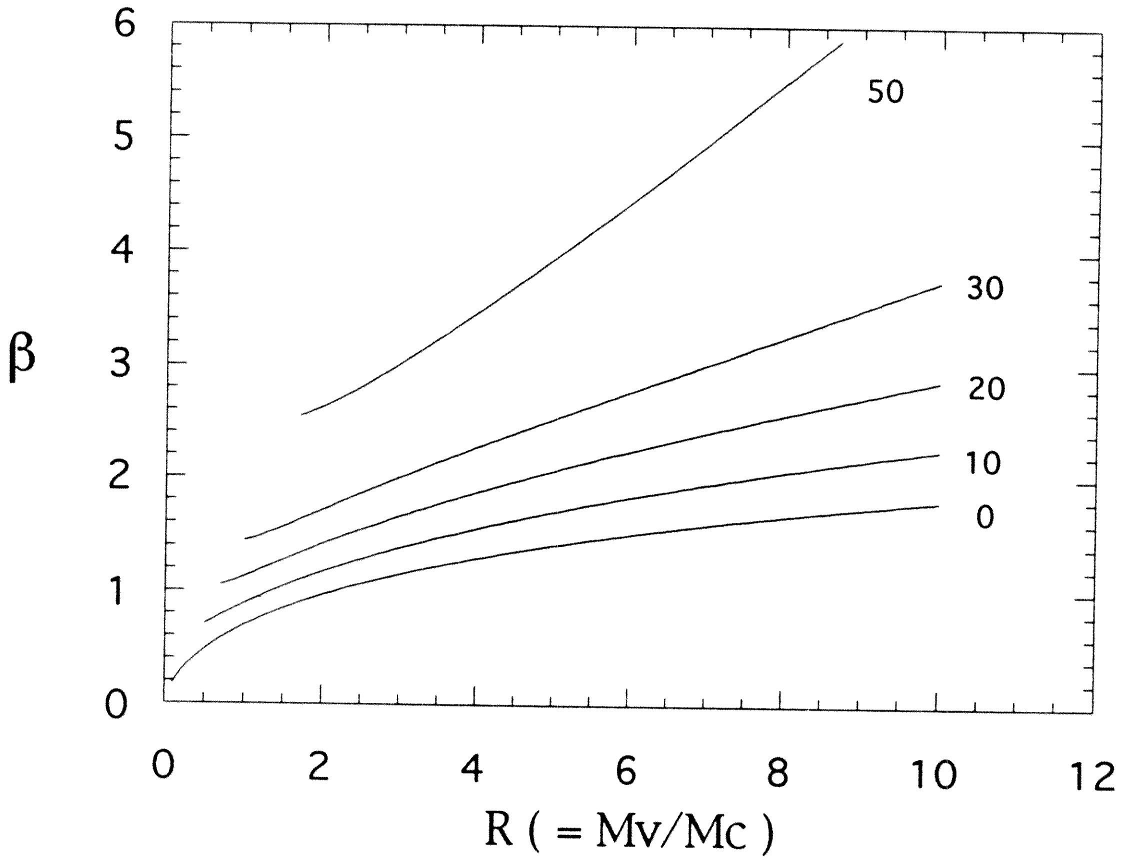

Figure 6.3: Calculated threshold temperature sensitivity factor β for various threshold gain as a function of valence/conduction band effective mass.

corresponds to a high injection level and higher subband population can no longer be neglected. $\beta(R)$ is shown for threshold gains of 10, 20, 30, and 50 cm^{-1}. The transparency value (gain = 0) is also shown and coincides with the plot of $\alpha(R)$, which is just $\beta(R)$ calculated for the transparency condition, in reference [10].

6.5 Threshold Current vs. Temperature

The threshold current density, J_{th}, is related to n_{th} and can be expressed in terms of the recombination coefficients

$$J_{th} = eL_z n_{th}(A(T) + n_{th}B(T) + {n_{th}}^2 C(T)) \tag{6.9}$$

At low temperatures and carrier densities, the radiative component of the current density is dominant [13] and we approximate (9) by neglecting A and C. We arrive at an expression for the threshold current density as a function of effective mass ratio and bimolecular recombination constant B,

$$J_{th} = eL_z \beta^2(R) n_c^2 B(T) \tag{6.10}$$

or using the expression for n_c ,

$$J_{th} = e(L_z \rho_c k_b T)^2 \beta^2(R) B(T). \tag{6.11}$$

Now, B(T) is a function of temperature, density of states, and the dipole matrix element describing the transition. For the case of non-degenerate bands, using k-selection rules, B(T) has been solved for analytically [3], and for the quantum well case, was shown to be inversely dependent on temperature. Also, experimental results [13] indicate a T^{-1} dependence of B. Substituting this form of B into (11), and neglecting any band structure dependence of B, we obtain

$$J_{th} = C_1 \beta^2(R) T \tag{6.12}$$

which is our final result. C_1 is a constant (we neglect the band structure dependence of B) and the slope of the transparency current with temperature, $\frac{dJ_{th}}{dT}$, is determined by the valence/conduction band mass ratio through the factor $\beta(R)$.

If we use this model of laser threshold, we find a good agreement between the ratio of measured $\frac{dI_{th}}{dT}$. Calculations [14,15] predict, for strained InGaAs, a valence band effective mass of $0.08 - 0.09 m_0$ whereas measurements [15] indicate a value of $0.14 m_0$. Using $R = 2$ for InGaAs and $R = 8$ for unstrained GaAs we calculate a slope ratio, $(\frac{\beta_{GaAs}}{\beta_{InGaAs}})^2$. Table 6.2 shows the value of the slope ratio for various threshold gains. we see that for low threshold gain, the slope ratio is calculated to be 3, which agrees well with the measured value of 2.5.

6.6 Conclusions

In conclusion, we have demonstrated $120 \mu A$ and $165 \mu A$ threshold currents in GaAs and InGaAs lasers, respectively, at cryogenic temperatures. We have measured the lasing threshold current and wavelength of GaAs and strained InGaAs lasers for temperatures between $5 - 300° K$ and, consistent with existing models[3,7], the threshold currents increase linearly with increasing temperature. The InGaAs laser is less sen-

g_{th} [cm^{-1}]	0	10	20	30	50
$\beta(8)/\beta(2)$	3.01	3.11	3.28	3.62	4.4

Table 6.2: Calculated values of $\beta^2(R)$ for various threshold gains

sitive to temperature variations at these low temperatures, which we attribute to a reduced valence band effective mass. We have proposed a simple model to explain the difference in $\frac{dI_{th}}{dT}$ for the two laser types which agrees well with our findings.

References

[1] J. Pankove, *Optical Processes in Semiconductors*, Dover, New York (1975)

[2] N.K. Dutta, *Electron. Lett.* **18**, 451 (1982)

[3] A. Haug, *Appl. Phys. B* **44**, 151 (1987)

[4] M.M. Leopold, A.P. Specht, C.A. Zmudzinski, M.E. Givens, and J.J. Coleman, *Appl. Phys. Lett.* **50**, 1403 (1987)

[5] J. Nagle, M. Hersee, T. Weil, and C. Weisbuch, *Appl. Phys. Lett.* **49**, 1325 (1986)

[6] S.R. Chinn, P.S. Zory, and A.R. Reisinger, *IEEE J. Quantum Electron.* **24**, 2191 (1988)

[7] P. Blood, E.D. Fletcher, K. Woodbridge, K.C. Heasman, and A.R. Adams, *IEEE J. Quantum Electr.* **25**, 1459 (1989)

[8] P. Blood, S. Colak, and A.I. Kucharska, *Appl. Phys. Lett.* **52**, 599 (1988)

[9] T. Bartolac, Aerojet Corp., private communication

[10] L.E. Eng, A. Sa'ar, T.R. Chen, I. Grave, N. Kuze, and A. Yariv, *Appl. Phys. Lett.* **58**, 2752 (1991)

[11] L.E. Eng, T.R. Chen, S. Sanders, Y.H. Zhuang, B. Zhao, H. Morkoç, and A. Yariv, *Appl. Phys. Lett.* **55**, 1378 (1989)

[12] K. Lau, S. Xin, W.I. Wang, N. Bar-Chaim, and M. Mittelstein, *Appl. Phys. Lett.* **55**, 1173 (1989)

[13] A.P. Mozer, S. Hausser, and M.H. Pilkuhn, *IEEE J. Quantum Electron.* **21**, 719 (1985)

[14] I. Suemune, L.A. Coldren, M. Yamanishi, and Y. Kan, *Appl. Phys. Lett.* **53**, 1378 (1988)

[15] J.E. Schirber, I.J. Fritz, and L.R. Dawson, *Appl. Phys. Lett.* **46**, 187 (1985)